Nitric oxide modulates contrast suppression in a subset of mouse retinal ganglion cells

Dominic Gonschorek[1-3], Matías A. Goldin[5], Jonathan Oesterle[1,2], Tom Schwerd-Kleine[1-3], Ryan Arlinghaus[1,2], Zhijian Zhao[2], Timm Schubert[1,2], Olivier Marre[5], and Thomas Euler[1-4,✉]

[1]Werner Reichardt Centre for Integrative Neuroscience, University of Tübingen, Tübingen, Germany
[2]Institute for Ophthalmic Research, University of Tübingen, Tübingen, Germany
[3]GRK 2381 'cGMP: From Benchside to Bed', University of Tübingen, Tübingen, Germany
[4]Bernstein Center for Computational Neuroscience, University of Tübingen, Tübingen, Germany
[5]Institut de la Vision, Sorbonne Université, INSERM, CNRS, Paris, France

Neuromodulators have major influences on the regulation of neural circuit activity across the nervous system. Nitric oxide (NO) has been shown to be a prominent neuromodulator in many circuits and has been extensively studied in the retina. Here, it has been associated with the regulation of light adaptation, gain control, and gap junctional coupling, but its effect on the retinal output, specifically on the different types of retinal ganglion cells (RGCs), is still poorly understood. In this study, we used two-photon Ca^{2+} imaging and multi-electrode array (MEA) recordings to measure light-evoked activity of RGCs in the ganglion cell layer in the *ex vivo* mouse retina. This approach allowed us to investigate the neuromodulatory effects of NO on a cell type-level. Our findings reveal that NO selectively modulates the suppression of temporal responses in a distinct subset of contrast-suppressed RGC types, increasing their activity without altering the spatial properties of their receptive fields. Given that NO release is triggered by quick changes in light levels under photopic conditions, we propose that these RGC types signal fast contrast changes to higher visual regions. Remarkably, we found that about one-third of the RGC types, recorded using two-photon Ca^{2+} imaging, exhibited consistent, cell type-specific adaptational response changes throughout an experiment, independent of NO. By employing a paired-recording paradigm, we could disentangle those additional adaptational response changes from drug-induced modulations. Taken together, our research highlights the selective neuromodulatory effects of NO on RGCs and emphasizes the need of considering non-pharmacological activity changes, like adaptation, in such study designs.

retina | ganglion cells | nitric oxide | neuromodulation
Correspondence: ***thomas.euler@cin.uni-tuebingen.de***

Introduction

The retina can be considered as a visual signal processor with a straightforward functional architecture (1–3). The photoreceptors convert the stream of photons from the environment into an electrical signal, which is relayed downstream by the bipolar cells (BCs) to the retinal ganglion cells (RGCs), the tissue's output neurons. Along this vertical pathway, the visual signal is shaped by two lateral, inhibitory cell classes: horizontal cells in the outer and amacrine cells (ACs) in the inner retina. The resulting intricate networks allow sophisticated computations, reflected in the >40 output channels that relay diverse visual feature representations as spike trains to higher brain regions (4–6).

Over the past decades, the retinal synaptic networks have been intensively studied, which greatly broadened our understanding of early visual signal processing (7–12). Specifically, the availability of connectome data for large parts of the retina helped in unprecedented ways, as can be seen from studies, for example, investigating direction-selective circuits and their precise wiring regarding starburst ACs and direction-selective RGCs (e.g., (13, 14)).

What is not well-captured by connectomic approaches are 'wireless' interactions mediated by neuromodulators, which comprise a broad variety of very different small molecules, including monoamines (e.g., dopamine (15, 16), histamine (17, 18), serotonin (19)), endocannabinoids (20–22), gasotransmitters such as nitric oxide (NO) (23, 24)), as well as a variety of neuropeptides (e.g., neuropeptide Y (25, 26)). Only few of the >20 neuromodulators (27) found in the retina are released from centrifugal fibers (e.g., histamine and serotonin (17–19, 28)), whereas most of them are released in addition to GABA or glycine by ACs (27, 29–32). Neuromodulators have long been implicated in adapting the retina to different contextual states necessary to robustly perform in a highly dynamic visual environment (e.g., (33–36)). For instance, dopamine (DA) is released by a distinct type of AC (37–40), and has been shown to regulate light adaptation (33, 41, 42) via several cellular mechanisms, such as modulation of gap junctional coupling (34, 43–45) and intrinsic conductances (46, 47). More recently, histamine was proposed to shape the retinal code in a top-down modulatory manner related to the animal's arousal state (17, 28). For several neuromodulators, the retinal release sites and receptors are known and their effects on cellular properties have been described, however, a comprehensive, function-oriented, and cell-type view of these neuromodulators' functional implications and contributions to visual signal processing is only slowly emerging (e.g., (17, 48)).

One of the better-studied neuromodulators in the retina is NO. Neuronal nitric oxide synthase (nNOS) is considered the dominant enzyme producing NO relevant for retinal signal processing, and – depending on species – was shown to be present in different retinal cell classes (49–57). In the mouse retina, nNOS was mainly found in specific AC types (36, 58–60). A few years ago, Jacoby et al. (36) demon-

strated that one of those types (nNOS2-AC) controls the light-dependent release of NO in the inner retina. NO can function via two main pathways (61): (*i*) it can bind to the NO guanylate cyclase (NO-GC; also referred to as soluble guanylate cyclase (sGC)) receptor, triggering the production of the second messenger cyclic guanosine monophosphate (cGMP), which binds to downstream targets (55, 62, 63), and (*ii*) via S-nitrosylation (cGMP-independent) by directly modifying certain receptor and channel proteins (64, 65).

The effects of NO have been primarily linked with light adaptation and the transition between scotopic and photopic signaling pathways via several mechanisms, including uncoupling the gap junctions between AII ACs and On-cone BCs (66), increasing the gain of On-cone BCs in response to dim light (67, 68), and modulating the gain of Off-cone BCs (69, 70). At the retina's output level, increasing NO was found to decrease On- and Off-responses in RGCs (71). Notably, genetically knocking out nNOS also led to a reduced light sensitivity in RGCs (72), which was also shown by inhibiting nNOS under light-adapted conditions (73). Additionally, NO has been shown to modulate RGC responses via cGMP by altering their cGMP-gated conductances (74, 75). Taken together, NO can act on different levels and via different pathways in the retina. However, the function of NO at the cell type-level and its role in early visual processing is far from understood.

Here, we systematically studied the functional role of NO and its effects on all retinal output channels in the *ex vivo* mouse retina. Surprisingly, we observed highly reproducible, cell type-specific changes in the light responses of some RGCs already in the absence of pharmacological manipulation. To account for these adaptational response changes, we developed a recording paradigm to measure 'paired' RGC responses under control and drug conditions. We found that NO had a highly selective effect on a distinct set of three RGC types characterized by their suppressed response to temporal contrast, where NO strongly and differentially reduced this suppression, as well as caused them to respond faster. Yet, NO had no discernible effects on their spatial receptive field properties. Together, our data suggest that NO modulates the visual feature representation of the retinal output in a highly selective and type-specific manner.

Results

To investigate NO effects systematically on the retinal output, we performed population imaging from somata in the ganglion cell layer (GCL) of *ex vivo* mouse retina electroporated with the synthetic Ca^{2+} indicator Oregon Green BAPTA-1 (Fig. 1a-c; Methods). In addition, we recorded a complementary dataset using multi-electrode array (MEA) recordings. To identify the different types of RGCs and detect potential NO-induced response changes, we presented a set of visual stimuli, including full-field chirps, moving bars (Fig. 1d), and binary dense noise (5) (see Methods).

A protocol for 'paired' control/drug recordings. Previous studies have shown that retinal responses recorded with two-photon Ca^{2+} imaging can be systematically affected by experimental factors, such as excitation laser-induced activity, photoreceptor bleaching, and temporal filtering due to Ca^{2+} buffering by the fluorescent indicator (76–78). These changes can be summarized by the umbrella term 'batch effects' (a term coined in the molecular genetics field), which can confound the biological signal and potentially cause erroneous interpretations of the data (78, 79). Such batch effects may play a role when, as in our study, data are recorded in a sequential manner to infer possible drug effects.

Because we wanted to detect potentially subtle NO effects, we devised a protocol to make experiments as comparable as possible (Fig. 1e). After placing the tissue into the recording chamber, it was allowed to recover from the electroporation for 15 min, before we light-adapted the retina for 10 min by presenting the dense noise stimulus. We then selected retinal recording fields, each of which was recorded twice for the complete stimulus set in an interlaced manner (Fig. 1e). The first field was recorded twice without perturbation (*control-control pair*). For the next field, we added the drug to the perfusion medium and incubated the tissue for ∼15 min, before recording the field for the second time (*control-drug pair*).

Using this protocol, we recorded the following paired datasets: (*i*) a control dataset to test response stability, i.e., Ctrl 1 and Ctrl 2, (*ii*) a strychnine dataset to test the protocol for a drug with well-described effects, i.e., Ctrl 1 and Strychnine (1 µM), and *(iii)* a NO-dataset to infer NO-induced response changes, i.e., Ctrl 1 and NO (DETA/NO; 100 µM). The control dataset was leveraged to reveal NO-induced effects on the background of potential nonspecific response changes throughout the experiment. For the following analyses, we used 3,975 paired RGCs (n_{Ctrl}=1,701; n_{NO}=1,838, $n_{strychnine}$=436) that fulfilled our response quality filtering (see Methods).

Identifying functional RGC types using a classifier. The mouse retina contains more than 40 RGC types (5, 6). As we wanted to investigate if the tested drugs differentially affect the different retinal output channels, we applied an RGC type classifier (Fig. 2a) (80), which had been trained and validated on a previously published RGC Ca^{2+} imaging dataset (5). The classifier predicts a GCL cell's functional type based on soma size and the responses to chirp and moving bar stimuli (see Methods). The classifier also distinguishes between RGCs and displaced ACs. Here, we focused our analysis on the RGCs. To match the conditions under which the classifier's training data was acquired as closely as possible, we predicted types based on the responses from the first control recording (Ctrl 1). To minimize classification uncertainty, we additionally discarded cells with low confidence scores (< 0.25, see Methods for details).

We found that the distributions of the predicted RGC types in our datasets matched that of the earlier dataset quite well (Fig. 2b-d). Also, the predicted mean traces for the individual RGC types were very similar to those in Baden

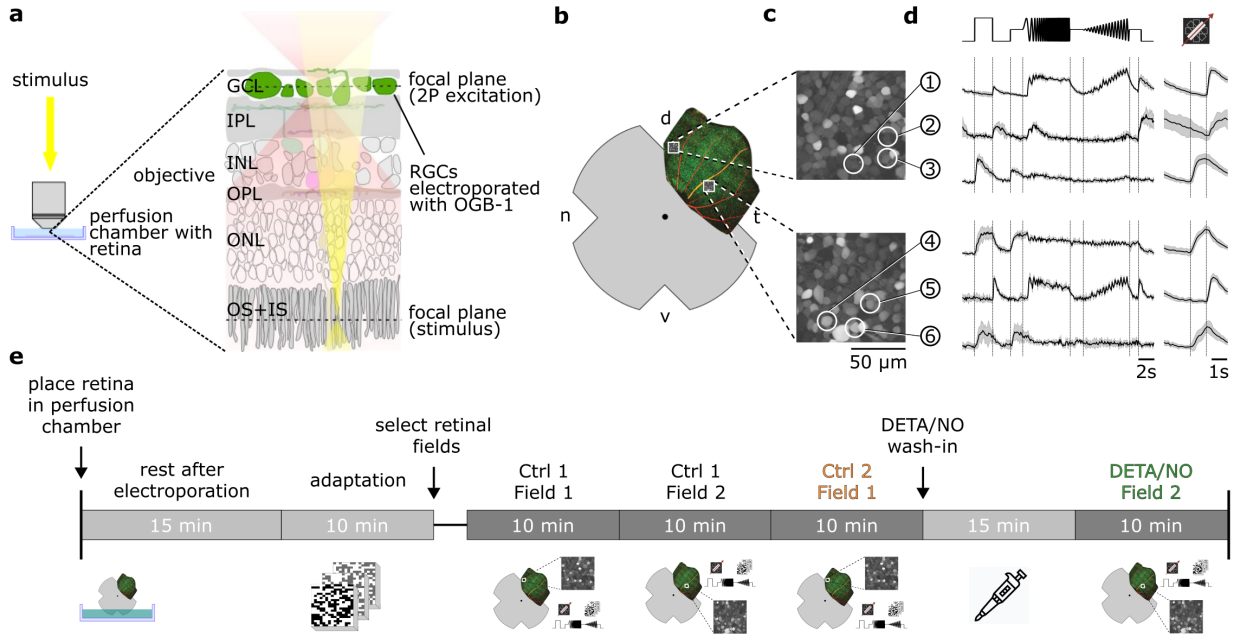

Fig. 1. Overview of the experimental setup and recording procedure. (**a**) Two-photon imaging of ganglion cell layer (GCL) somata in the whole-mounted mouse retina. (**b**) Schematic *ex vivo* whole-mounted retina (dot marks optic disc; d, dorsal; t, temporal; v, ventral; n, nasal). (**c**) Two representative recording fields from (b) showing GCL somata loaded with Ca^{2+} indicator OGB-1 (Methods). (**d**) Representative Ca^{2+} activity from cells in the GCL (white circles in (c)) in response to chirp (left) and moving bar stimulus (right) (black, mean; gray, s.d.). (**e**) Timeline of experimental procedure; for details, see text. IPL, inner plexiform layer; INL, inner nuclear layer; OPL, outer plexiform layer; ONL, outer nuclear layer; OS+IS, outer and inner segments; DETA/NO, nitric oxide (NO) donor.

et al. (5) (Fig. 2e), as indicated by the high correlations of their chirp and moving bar responses (Fig. 2f left and right, respectively). That the moving bar responses were more strongly correlated than the chirp responses is likely due to the lower complexity and shorter duration of the former stimulus. Nonetheless, we found the RGC classification overall to be robust and comparable to the original dataset (Fig. S1a,b).

Testing and evaluating the recording protocol. To test our recording protocol, we used the glycine receptor antagonist strychnine (Fig. S2). In the mouse retina, glycine is released by small-field ACs and relays inhibition vertically across the inner plexiform layer (IPL; (32, 81)). For instance, such cross-over inhibition mediated by AII ACs relays the signals from rod BCs to Off-cone BCs, which is why strychnine eliminates Off RGC responses in dark-adapted retina (82). In the light-adapted retina, On-cone BCs boost light-Off responses in Off-cone BCs through cross-over inhibition (83, 84) and hence, strychnine affects Off-response components in RGCs – in line with our observations (Fig. S2): Strychnine application revealed additional On-responses in Off (e.g., G_1, G_2) and On-Off RGCs (e.g., G_{12}), as can be seen, for instance, in their leading-edge response to the moving bar (Fig. S2; left panel, middle column). In On RGCs, we did not detect substantial response changes with strychnine (Fig. S2; e.g., G_{17}).

Together, the strychnine dataset showcases that we can resolve drug-related effects on light responses at cell type-level.

Certain RGC types display adaptational response changes. To test if our recording conditions were stable and to exclude major batch effects, we first compared the responses of the control datasets (Ctrl 1 vs. Ctrl 2). To this end, we computed the difference between the Ctrl 1 and Ctrl 2 mean responses ($\Delta R_{(Ctrl2-Ctrl1)}$) to chirp and moving bar stimuli for each cell of every RGC type. This allowed us to quantify if and how the responses changed over the time course of an experiment (cf. protocol in Fig. 1e). Here, we only considered RGC types with >10 paired cells (21/32).

Surprisingly, while the majority of RGC types featured stable responses (e.g., G_1, G_{21}; Fig. 3a), a substantial number of RGC types (∼34%) changed their responses to chirp and/or moving bar stimuli in the absence of any pharmacological perturbation in a highly reproducible manner (Fig. 3b). For instance, for Ctrl 2, G_{23} showed reduced responses, whereas G_{31} showed an increased response activity. Interestingly, cells assigned to the functional groups of 'Off' RGC types displayed stable responses, whereas 'On-Off', 'Fast On', 'Slow On', and 'Uncertain RGCs' included types with changing responses (50% (2/4), 34% (1/3), 67% (4/6), and 67% (2/3), respectively). This diversity argues against a systematic effect (such as, e.g., general run-down) and for a cell type-specific phenomenon, which in the following we refer to as 'adaptational response changes'.

NO affects retinal output in a highly type-specific manner. Next, we investigated the effects of NO on the RGC responses. As with the control dataset, we computed the cell-wise response differences between Ctrl 1

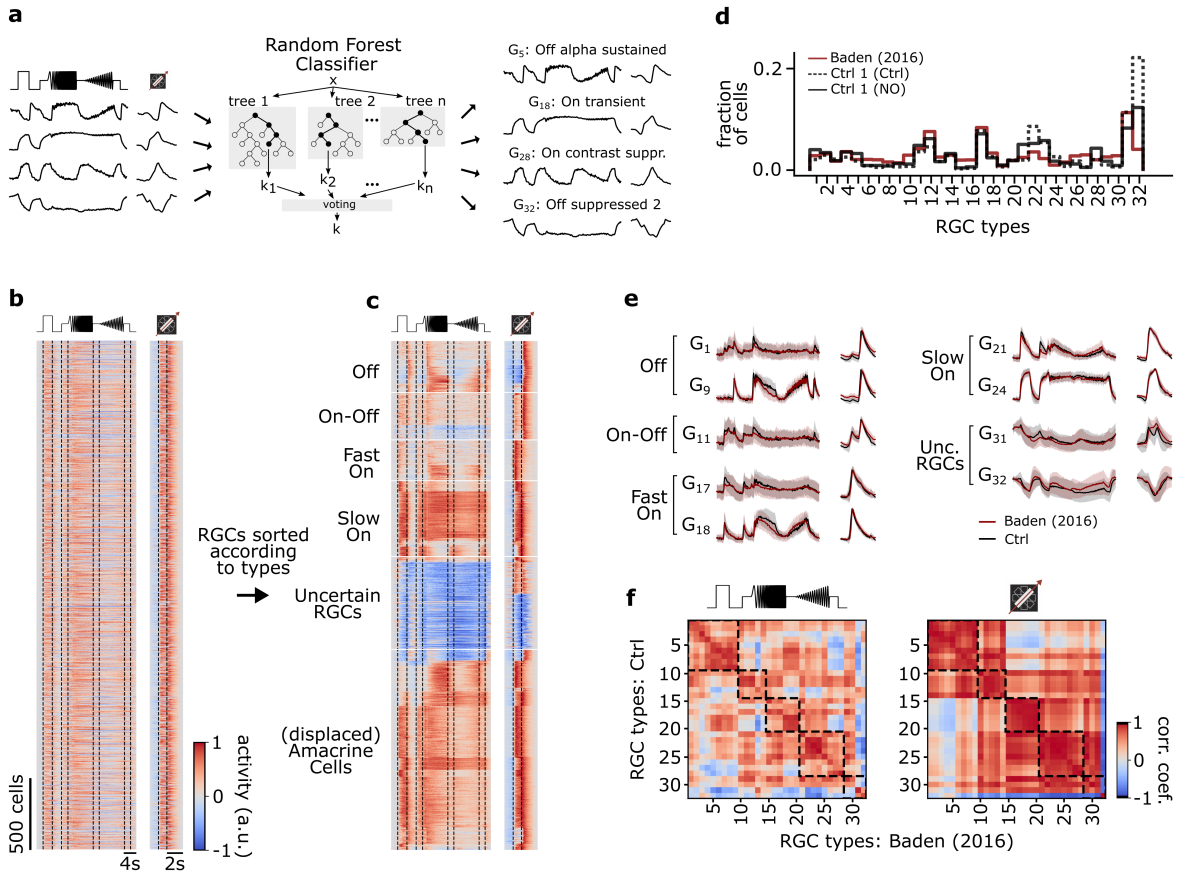

Fig. 2. Functional classification of mouse RGC types. (**a**) Illustration of the random forest classifier (RFC) to predict cell type labels for Ctrl 1 of both datasets. For each cell, Ca^{2+} responses to chirp and moving bar, soma size, and p-value of permutation test for direction selectivity (left) constitute the input to the RFC (center) to predict a cell type label, i.e., a type G_X (right). For details, see Methods and (80). (**b**) Pooled heat map of unsorted cell responses to chirp and moving bar stimulus from both Ctrl 1 datasets after quality filtering (QI_{MB}>0.6 or QI_{chirp}>0.45, and classifier confidence score ≤ 0.25). The color bar indicates normalized response activity. (**c**) Heat map from (b), but sorted according to their assigned type. (**d**) Distribution of RGC types predicted by the RFC classifier for both Ctrl 1 of control pair (Ctrl 1 (Ctrl); solid black), of DETA/NO pair (Ctrl 1 (NO); dotted black), and for the dataset from Baden et al. (5) (red). (**e**) Representative RGC type response averages to chirp and moving bar (Ctrl, black; training dataset, red). (**f**) Correlation matrix of type mean responses per RGC type between Ctrl and dataset for chirp (left) and moving bar (right). Dashed boxes indicate functional groups (Off, On-Off, Fast On, Slow On, and Uncertain RGCs; see (5)). The color bar indicates the Pearson correlation coefficient.

and NO responses ($\Delta R_{(NO-Ctrl1)}$). Similar to the control dataset, the majority of RGC types displayed stable responses (e.g., G_2, G_{17}; Fig. 3c), while ∼43% changed their responses significantly (e.g., G_{28}, G_{32}; Fig. 3d) following the NO perfusion. We found that the percentage of changing types per functional group was similar to that in the control dataset: 'Off' (0% (0/5)), 'On-Off' (50% (2/4)), 'Fast On' (34% (1/3)), 'Slow On' (66% (4/6)), and 'Uncertain RGCs' (66% (2/3)). This raised the question if the observed changes in the NO-dataset indeed reflected NO-induced modulations or mostly adaptational response changes (as observed in the control dataset). We, therefore, tested for each RGC type if the response changes observed for control ($\Delta R_{(Ctrl2-Ctrl1)}$) and NO ($\Delta R_{(NO-Ctrl1)}$) were significantly different (Fig. 3e). To our surprise, this was only the case for two types: (1) G_{32} ('Off suppressed 2') RGC, which is characterized by a high baseline activity that is strongly suppressed below baseline during light increments and displays increased activity during light decrements, and (2) G_{18}, which is considered as being a 'Fast On' type having a response to light increments with a fast response kinetic. This suggests highly type-selective NO effects – at least for temporal responses to chirp and moving bar stimuli.

Next, we leveraged the control dataset to disentangle NO-induced from adaptational effects at the level of the response features. To this end, we subdivided the chirp stimulus into six feature segments ((1) On, (2) Off, (3) low frequency, (4) high frequency, (5) low contrast, (6) high contrast), and the moving bar into two ((7) On, (8) Off) (Fig. 4c). Then, for every cell type and every response feature, we computed the difference of the mean responses between the first and second recording separately for the control (Fig. 4a; left panel) and NO-dataset (Fig. 4a; middle panel). To isolate NO-induced effects, we computed the differences ($\Delta R_{(NO-Ctrl1)} - \Delta R_{(Ctrl2-Ctrl1)}$; Fig. 4a; right panel), based on the assumption that the adaptational component of the changes would be similar for both datasets. Through this analysis, we found three response behaviors across the RGC types: (1) not NO-affected/stable, (2) showing adaptational cell type-specific changes, and (3) NO-affected (Fig. 4b).

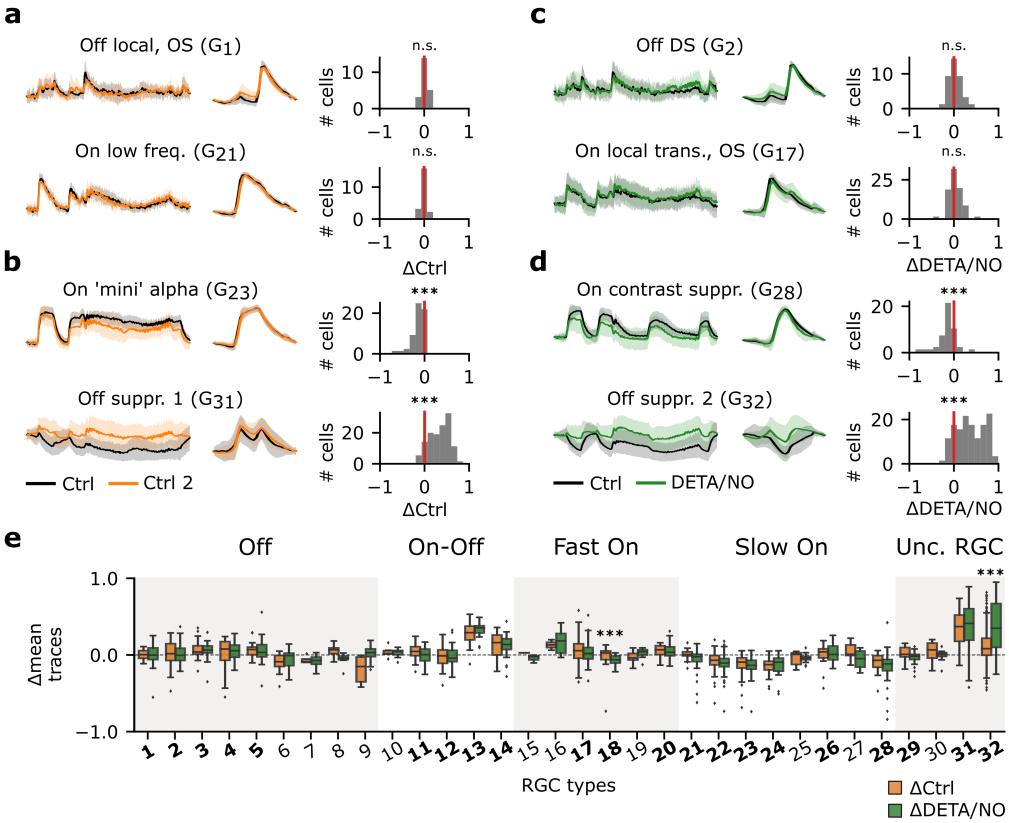

Fig. 3. Certain RGC types are affected by adaptational and/or NO-induced effects, while others are unaffected. (**a**) Left: Two representative mean Ca^{2+} responses of paired RGC types showing no differences between Ctrl 1 (black) and Ctrl 2 (orange) (top: G_1; bottom: G_{21}). Right: Corresponding histograms displaying the trace differences between paired cell responses of the respective cell types. Zero indicates no difference between the response of the same cell across both recordings, whereas negative values indicate a decreased and positive values an increased activity. n.s.: not significant; ***: p<0.001; One-sample T-test. (**b**) Two representative RGC types that show decreased (top: G_{23}) and increased (bottom: G_{31}) response activity during Ctrl 2. n.s.: not significant; ***: p<0.001; One-sample T-test. (**c**) As in (a), but between paired Ctrl 1 (black) and DETA/NO (green) (top: G_2; bottom: G_{17}). n.s.: not significant; ***: p<0.001; One-sample T-test. (**d**) As (c), but showing two cell types that display a decreased (top: G_{28}) and increased (bottom: G_{32}) activity when perfused with DETA/NO. n.s.: not significant; ***: p<0.001; One-sample T-test. (**e**) Box plots of trace differences of all paired cells of all RGC types from control (Ctrl 1 & Ctrl 2; orange) and NO-dataset (Ctrl & DETA/NO; green). Bold numbers indicate RGC types with >10 paired cells per dataset and condition. Dashed line shows zero baselines, i.e., no difference between traces. Gray and white background blocks summarize the larger functional groups for better visualization (Off, On-Off, Fast On, Slow On, Uncertain RGCs). ***: p<0.001; Mann-Whitney U-Test.

As before, we found that G_{32} is strongly affected by NO; it showed barely any adaptational response changes, yet its activity increased during NO application (Fig. 4b; (3)). This increase in activity was statistically significant for the chirp's On (1) and Off steps (2) and during both the frequency and contrast modulations ((3)-(6)), as well as for the moving bars trailing edge (8) (for tests, see Fig. 4 legend), suggesting that NO reduces the cell's inhibition by temporal contrast.

Interestingly, a cell type from the same larger functional group that features analogous response properties, G_{31} ('Off suppressed 1'), displayed a similar behavior during the NO application (Fig. 4a). However, G_{31} showed this response change for most features already in the control, suggesting that this effect was primarily adaptational (Fig. 4a; right panel). Still, our analysis suggests that NO had a significant effect, though different from what we observed for G_{32}: in G_{31} the response to the chirp's Off step (2) increased, whereas that to the moving bar's leading edge (7) decreased. Note that it is possible that additional NO effects on G_{31} may have been 'masked' by the strong adaptational response changes.

In the previous analysis, G_{18} showed significant differences between the control and NO-dataset, but this effect was not mirrored by the feature-wise analysis, indicating that a potential effect may be much weaker compared to the effect NO has on G_{32}. Notably, RGC types that were assigned to the group of the so-called 'Slow On' types (G_{21}-G_{28}), which exhibit strong and sustained responses during the frequency and contrast sequences of the chirp stimulus, showed a decrease in activity in both datasets (e.g., G_{24}; Fig. 4b; (2); bottom). Consequently, the changes in these response features ((3)-(6)) are likely adaptational (Fig. 4a) – as the changes can be found in the control (Fig. 4a; left panel) as well as in the NO-dataset (Fig. 4a; middle panel), but not in the difference (Fig. 4a; right panel). Our conclusion that both adaptational and NO-mediated effects on RGC responses are highly cell type-selective is further supported by the fact that we also found several RGC types that showed stable responses during control and NO application (Fig. 4b; (1)).

Taken together, our analysis revealed that the adaptational and NO-induced effects occurred on a feature-specific as well as cell type-specific level. On the one hand, several 'Slow On' types showed adaptational effects in response to temporal frequency and contrast features, while other features were not affected. On the other hand, at least one distinct RGC type (G_{32}) displayed a significantly increased response modulation of most features during the NO application; hence hinting towards an effect of NO on response suppression, as in the case of G_{32} is elicited by temporally changing stimulus contrast. Consequently, we focused on a more in-depth analysis of NO-induced effects on G_{32}.

Clustering of G_{32} responses reveals three functionally distinct RGC types with different NO-sensitivity. According to Baden et al. (5), G_{32} features a coverage factor of $\sim$4. As the average coverage factor of mouse RGCs was estimated to be $\sim$2 (5, 85), G_{32} likely consists of several (functional) RGC types. This may be supported by the high variation of G_{32} responses, which also supports the presence of several types (see Fig. 3e). To test this, we performed Mixture of Gaussians clustering of RGCs assigned as G_{32} (Fig. 5a-c) using the Ctrl 1 responses to chirp and moving bar stimuli from both datasets (Fig. 5a). We found three distinct clusters – all suppressed-by-contrast but to different degrees (Fig. 5d,e).

All three G_{32} clusters showed little adaptation for the control dataset, but displayed differential modulations in response to NO application, with cluster 1 exhibiting the strongest NO effect (Fig. 5f,g; left) for both stimuli. The NO effect was statistically significant in clusters 1 (n=134) and 2 (n=126) – both for mean trace difference and correlation (Fig. 5g; left and right, respectively) – but only for trace correlation in cluster 3 (n=77).

Since the prominent feature of these RGC types is suppression by temporal stimulus contrast, we compared their suppression strength between the conditions using a suppression index (SI; see Methods). Here, we found that in cluster 1, SI marginally, yet significantly, changed between Ctrl 1 and Ctrl 2, but was strongly and significantly reduced by NO as ΔSI were significantly different (Fig. 5h; top panel). Similar response behavior can be found in cluster 2, which displayed significant differences in SI and ΔSI in both control and NO-dataset (Fig. 5h; middle panel). In fact, with NO, these cells lost their suppressive feature and were rather excited than suppressed by the stimuli. In contrast, cluster 3 showed no significant differences of the SI between Ctrl 1 and Ctrl 2, but a clear modulation by NO (Fig. 5h; bottom panel).

Taken together, our data indicate that G_{32} may consist of three suppressed-by-contrast RGC types and that in at least two of them, the contrast suppression is strongly modulated by NO.

NO does not affect RGC receptive field properties. So far, we focused on effects in the temporal response domain, where we found that mainly G_{32} types were affected by an increase in NO levels. However, NO has been shown to affect electrical coupling, e.g., by reducing conductance between AII ACs and On-cone BCs (66), and hence may alter receptive field (RF) properties. Therefore, we next investigated the effects of NO on the spatial RFs (sRFs) of the individual RGC types. To this end, following the same experimental paradigm as described earlier, we recorded RGC responses to binary dense noise. Next, we computed their sRFs for both recording conditions (Fig. 6a) using spike-triggered averaging (86), obtaining control and NO sRFs, and then fitted a Gaussian to each sRF's center (Fig. 6a). We focused the following analysis on RGC types with reliable sRF estimates (see Methods). These included types in all five larger RGC groups (5): G_5 for 'Off'; G_{11}, G_{12}, and G_{14} for 'On-Off'; G_{17} for 'Fast On'; G_{23}, G_{24}, G_{26}, and G_{27} for 'Slow On'; G_{31} and G_{32} for 'Uncertain RGCs'. In these types, sRFs were very stable in both control and NO condition.

Using the difference in sRF center diameter between control and NO as a metric (Fig. 6b), we did not find NO to cause any significant changes in sRF size in any of the analyzed RGC types. Next, we tested if the sRF surround was affected by NO, because a modulation of inhibitory synaptic input and/or electrical coupling may cause a change in surround strength. As a measure of surround strength, we computed a surround index (see Methods) of control and NO sRFs (Fig. 6c). Like with the sRF center diameter, we did not find significant differences for any of the analyzed RGC types. Surprisingly, also G_{32} did not show NO-mediated differences in its sRF properties, implying that NO may only affect its temporal response, but not its RF organization.

Taken together, at least for the tested RGC types, we did not detect any significant NO effects neither on sRF center size nor surround strength.

NO affects the temporal response kinetics of G_{32} subtypes. The high spatial resolution of two-photon imaging allowed us to record and identify individual RGCs. However, it is limited by having a low temporal resolution to capture subtle temporal response dynamics, which led us to record a complementary dataset using MEA recordings. Since we found that the temporal response domain of G_{32} and its subtypes were affected by NO, MEA recordings enabled us to further investigate subtle neuromodulatory effects with a higher temporal resolution.

In particular, we recorded light-induced RGC responses (n=391) from four retinae under three consecutive conditions similar to the Ca^{2+}-dataset: *(i)* control, *(ii)* NO-donor (DETA/NO; 100 µM) and *(iii)* wash-out. As for the Ca^{2+}-dataset, we used the chirp stimulus for type identification as well as a checkerboard stimulus to estimate receptive fields. To identify and compare RGC types across the Ca^{2+}- and MEA-dataset, we clustered the RGC responses across retinae (Fig. 7a,b) and transformed their spike trains in response to the chirp stimulus into pseudo-calcium traces as described in Goldin et al. (87) (Fig. 7a; see Methods). Next, we matched the pseudo-calcium traces with the RGC types ob-

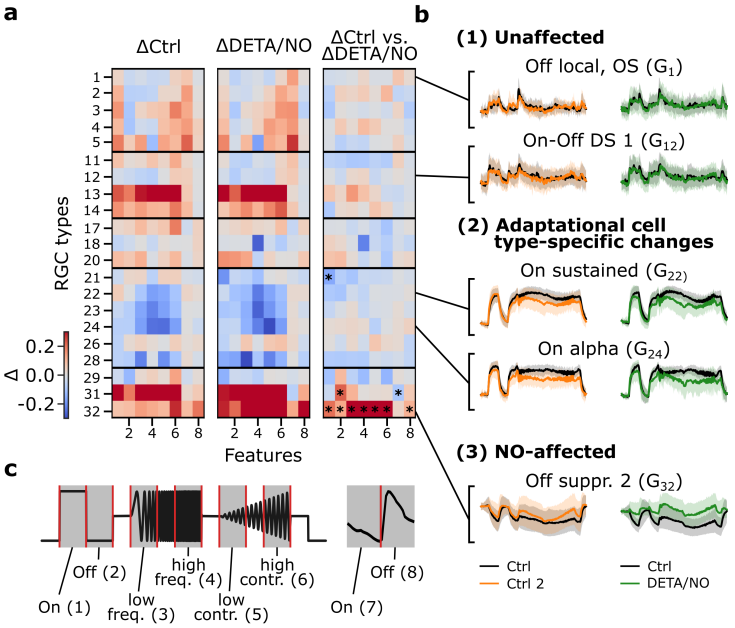

Fig. 4. Disentangling NO-induced effects from adaptational response changes reveals type-specific NO modulation. (**a**) Left: Difference between paired Ctrl 2 and Ctrl 1 RGC traces per type subdivided into 8 features ($\Delta R_{(Ctrl2-Ctrl1)}$). Color code indicates response increase (red), no change (white), and decrease (blue) for Ctrl 2. Middle: Difference between DETA/NO and Ctrl ($\Delta R_{(NO-Ctrl1)}$). Right: Difference between the two heatmaps ($\Delta R_{(NO-Ctrl1)} - \Delta R_{(Ctrl2-Ctrl1)}$). Asterisks indicate significant differences of the trace differences of all cells per feature and per cell type between $\Delta Ctrl$ and $\Delta DETA/NO$ using independent two-sided T-test and Bonferroni correction for multiple tests; *: p<0.0003. (**b**) Example chirp traces are categorized into unaffected (top two types: G_1, G_{12}), adaptational (two middle types: G_{22}, G_{24}), and NO-affected (bottom: G_{32}). Left traces show exemplary responses per type from the control dataset (black: Ctrl; orange: Ctrl 2) and NO-dataset (black: Ctrl; green: DETA/NO). (**c**) Subdividing the chirp (left) and moving bar (right) stimuli into 8 features for detailed feature analysis. The chirp is subdivided into 6 features ((i) on, (ii) off, (iii) low frequency, (iv) high frequency, (v) low contrast, and (vi) high contrast); the moving bar into 2 ((vii) on and (viii) off).

tained from Baden et al. (5) (Fig. 7d). Overall, we were able to record responses from all known RGC types, yet the sampling fractions for most types differ between the datasets, which can be explained by the recording bias inherent in MEA (88) (Fig. 7f).

As we found NO-induced response modulations in G_{32}, we focused on RGCs identified as such for the following analyses (n=42). We found that, similar to the Ca^{2+}-data (Fig. 5), G_{32} showed reduced suppression during NO-application (Fig. 8a; top), which is not present during the wash-out recording anymore, indicating that the NO-induced effect may be reversible (Fig. 8a; bottom). Since we found in our Ca^{2+}-dataset that G_{32} consists of three subtypes, we clustered these RGC types assigned as G_{32} into three clusters (Fig. 8b). For all subtypes, we found NO-induced response modulations showing a spectrum of their modulation strength and that the effects were reversible in the wash-out condition (Fig. 8c). As two-photon imaging only allows relatively short light stimulations, estimating precise receptive fields (RFs) can be difficult; hence we estimated spatial RFs (sRFs) and temporal RFs (tRFs) for the subclusters recorded with the MEA since it allowed us to display the checkerboard stimulus longer and to record individual spikes. Here, consistent with the Ca^{2+}-dataset, we did not find any NO-induced modulation of the sRF size in any of the clusters (Fig. 8d), yet the tRF kernels showed significantly faster response kinetics during NO-application for all three clusters (Fig. 8e). Also, the effects were reversible for two clusters (except for cluster 3). We did not find this effect in the Ca^{2+}-dataset (data not shown), which may be due to the low temporal resolution.

Taken together, our MEA-dataset confirmed and was in line with our Ca^{2+}-dataset that G_{32} consists of three types that were differentially modulated by NO. Also, we showed that indeed sRFs of those types were not affected by NO, but their suppression to temporal contrast. Additionally, the MEA-dataset revealed that all three types showed faster response kinetics induced by NO, which was reversible.

Discussion

We used two-photon Ca^{2+} imaging and MEA recordings to measure RGC responses to various visual stimuli to investigate the neuromodulatory effects of elevated NO levels on signal processing across RGC types in the mouse retina. To our surprise, even without pharmacological perturbation, we found that about one-third of the RGC types displayed highly reproducible and cell type-specific response changes during the course of an experiment – a finding of potentially high relevance especially for pharmacological experiments in the *ex vivo* retina using two-photon Ca^{2+} imaging. Accounting for these adaptational changes enabled us to isolate NO-related effects on RGC responses. Here, we revealed that mainly the RGCs assigned to G_{32} ('Off suppressed 2') were affected by NO, which strongly reduced the response suppression and rendered the cells more active. Further, we demonstrated that G_{32} likely consists of three types – consistent with its high coverage factor (5) – that were all differentially modulated by NO. Finally, for a repre-

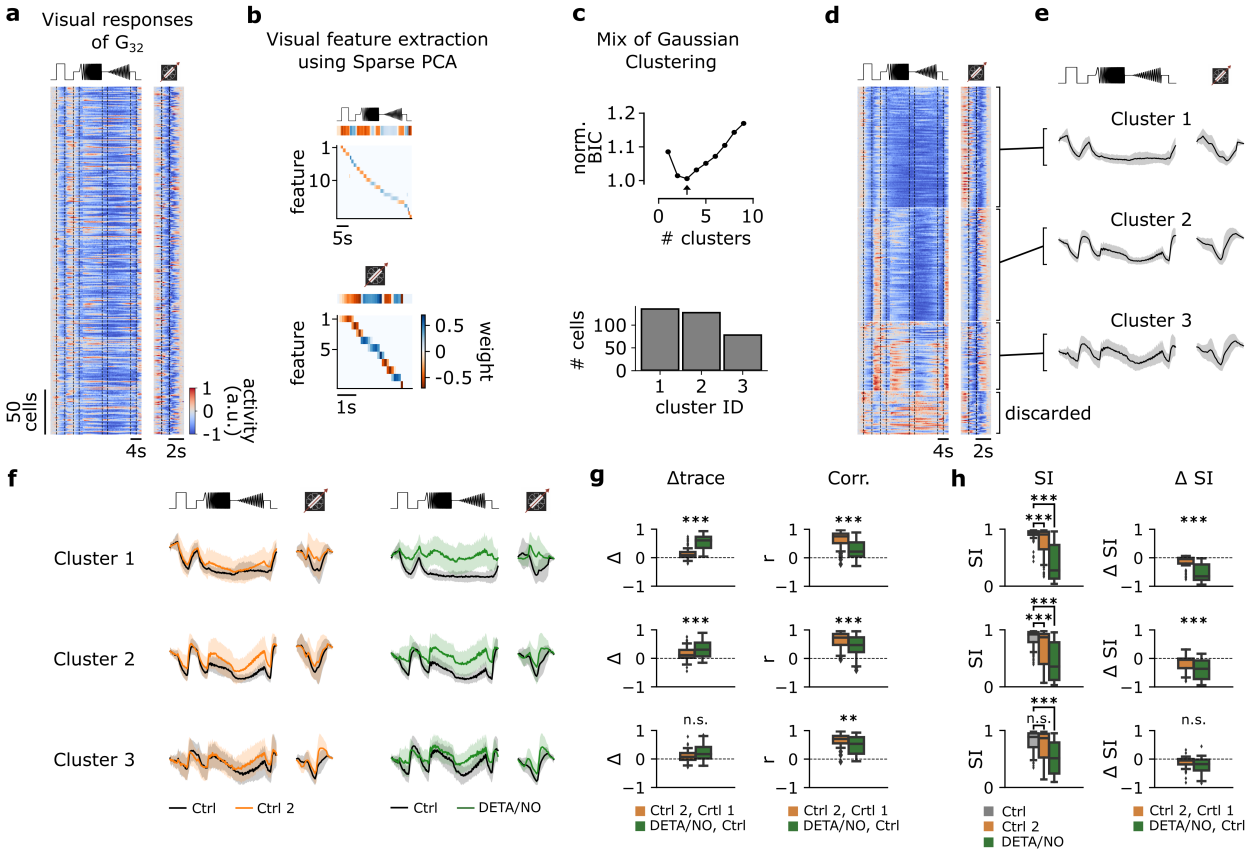

Fig. 5. Functional clustering of the G_{32} reveals three distinct types that are differently affected by NO. (**a**) Visual responses of G_{32} cells recorded from several experiments in response to the full-field chirp (left) and moving bar (right) stimuli. (**b**) Visual features extracted from chirp (top) and moving bar (bottom) stimuli using sparse PCA on the responses. Color indicates the weight of each feature. (**c**) Top: Bayesian Information Criterion (BIC) as function of number of clusters. Arrow indicates the lowest BIC and the number of clusters to choose. Bottom: Number of cells per predicted cluster. (**d**) Cells sorted according to their assigned cluster. Cells at the bottom were discarded. (**e**) Mean responses of the 3 corresponding clusters for the chirp (left) and moving bar (right). (**f**) Left: Paired mean responses of the 3 clusters to Ctrl 1 (black) and Ctrl 2 (orange). Right: Cluster mean responses to Ctrl 1 (black) and DETA/NO (green) (**g**) Left: Trace difference between Ctrl 2 & Ctrl 1 (orange) and DETA/NO & Ctrl (green) for the 3 clusters (clusters 1-3 from top to bottom). Right: Correlation coefficient between Ctrl 2 & Ctrl 1 (orange) and DETA/NO & Ctrl 1 (green) for the 3 clusters. n.s.: not significant; **: p<0.01, ***: p<0.001; independent T-test & Mann-Whitney U-Test. (**h**) Left: Suppression index (SI) computed for Ctrl 1 (gray), Ctrl 2 (orange), and DETA/NO (green) for the 3 clusters. n.s.: not significant; **: p<0.01, ***: p<0.001; Kruskal-Wallis test & Dunnett's test. Right: Difference of SI between Ctrl 2 & Ctrl 1 (orange) and DETA/NO & Ctrl 1 (green). n.s.: not significant; **: p<0.01, ***: p<0.001; independent T-test & Mann-Whitney U-Test.

sentative subset of RGC types, we showed that elevating the NO-level had no discernible effect on sRF size or surround strength. In addition, we were able to confirm those results using MEA recordings and showed that NO caused faster temporal response kinetics of these three subtypes; these changes were reversible. Together, our data suggest that NO specifically modulates response suppression and kinetics in a group of contrast-suppressed RGC types. Additionally, our study demonstrates the need for recording paradigms that take adaptational, non-drug-related response changes into account when analyzing potentially subtle pharmacological effects.

Nitric oxide as a (neuro-)modulator in the retina. Neuronal nitric oxide synthesis (nNOS) has been detected in different retinal cell classes (49–57) and the main NO-sensor (NO-GC), which connects NO to intracellular cGMP signaling (55, 60, 89, 90), is present in all retinal layers (70). This and earlier findings of NO modulating the response gain of BCs (68, 69) and RGCs (71) suggest that NO constitutes a neuromodulatory system within the retina involved in light adaptation. However, in the mouse retina, light-dependent NO production seems to mainly occur in specific AC types, with the nNOS2-AC being the main producer of endogenous NO (36). In particular, it releases NO in a fast manner, especially in response to light flicker (24, 36, 55, 60, 72). Thus, it has been suggested that this AC type is a suitable candidate to report fast contrast changes at photopic conditions (24, 36). Here, our results indicate that, in addition to serve for intrinsic light adaptation, NO also signals information about the visual environment, namely, fast-changing contrasts, from the retina to higher visual brain regions in a highly selective manner. Specifically, it modulates the functional response profile of a distinct group of likely three types of RGCs formerly amalgamated in G_{32} (5).

In particular, NO affected these types in a similar way, yet differentially by increasing their activity, partly eliminating their characteristic feature of being suppressed by temporal contrast and having faster response kinetics. Notably, the NO effect was only visible in their temporal responses; we did not detect changes in their sRF properties. This RGC type-selectivity of NO is reminiscent of a recent study,

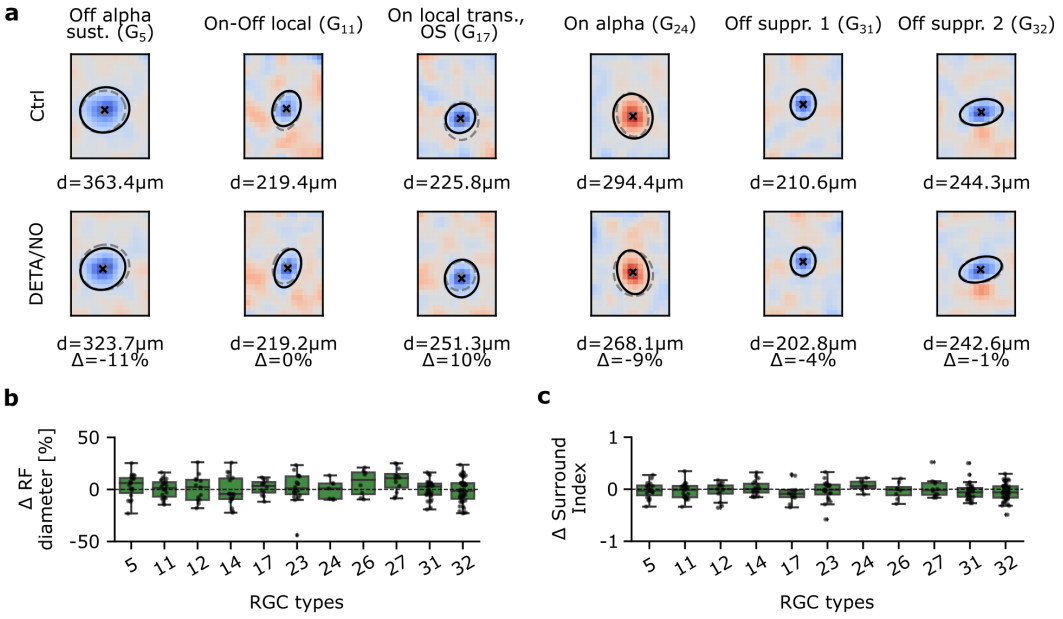

Fig. 6. Spatial receptive fields are not affected by NO across various RGC types. (**a**) Representative estimated spatial receptive fields (sRF) of six RGC types. Top: Estimated sRFs to Ctrl 1. Cross indicates RF center; solid line indicates outline of the Gaussian fit of the RF center; dashed outline indicates corresponding Gaussian fit of the same cell to DETA/NO. Bottom: Same as top, but of DETA/NO condition. (**b**) RF diameter difference in percentage between DETA/NO and Ctrl 1. Only types with more than 5 paired cells were included. One-sample T-test. (**c**) Surround index difference between DETA/NO and Ctrl 1. Only types with more than 5 paired cells were included. One-sample T-test.

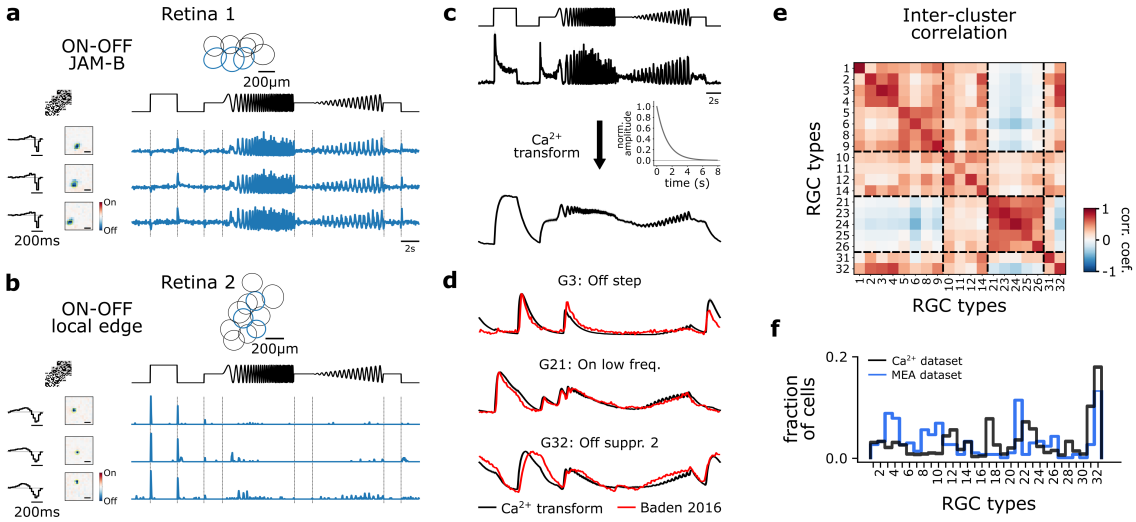

Fig. 7. Multi-electrode recordings and pseudo-calcium transformation. (**a**) Representative RGC type, 'On-Off JAM-B', recorded from one retina forming a mosaic. Three exemplary response traces of the same type. Cells are indicated in the mosaic as blue. Left: tSTAs and sSTAs computed from their responses to a checkerboard stimulus. Right: PSTHs to the chirp stimulus. (**b**) As **a**, but displaying another type, 'On-Off local edge'. (**c**) Illustration of the transformation of PSTHs to pseudo-Ca^{2+} traces using an OGB-1 filter described in Baden et al. (5) to match and identify RGC types. (**d**) Overlay of representative mean responses of three RGC types of the Baden et al. (5) dataset (red) and the assigned Ca^{2+}-transformed (black) traces to the chirp stimulus. (**e**) Inter-cluster correlation matrix of PSTHs of each assigned RGC type within a group with its group mean. Only types with >5 cells per type were included. Dashed boxes indicate functional groups (Off, On-Off, Slow On, and Uncertain RGCs; see (5)). Color bar indicates Pearson correlation coefficient. (**f**) Comparison of the distribution of predicted RGC types between the MEA (blue) and Ca^{2+} (black) datasets.

where the neuromodulator dopamine was found to modulate distinct response features of specific RGC subtypes (48).

To ensure reliable RGC type classification, our set of visual stimuli was restricted to artificial ones (full-field chirps, moving bars, and dense noise). Such artificial stimuli probe the stimulus space in a rather selective and limited fashion. Hence, we cannot exclude that we missed NO effects that may have become apparent for other, more complex stim-

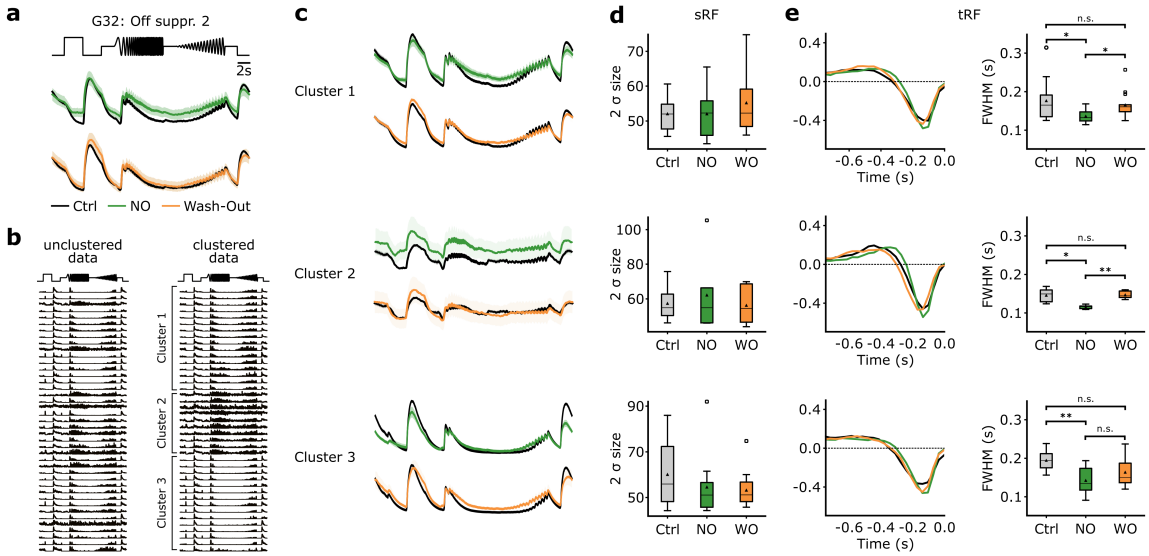

Fig. 8. NO only affects temporal features of three distinct clusters of G_{32}. (**a**) Mean Ca^{2+}-transform responses to the chirp of the RGC type G_{32}. Top: Paired RGC responses to the Ctrl (black) and DETA/NO (green) conditions. Bottom: Paired RGC responses to the Ctrl (black) and Wash-out (orange) conditions after DETA/NO application. (**b**) Left: Unclustered PSTHs of cells assigned to type G_{32}. Right: Cell's PSTHs were clustered and sorted into three distinct clusters. (**c**) Paired mean responses of the 3 clusters to Ctrl (black), DETA/NO (green), and Wash-out (orange). (**d**) Ellipse size of the fitted Gaussian of the sRF of the three conditions (Ctrl: black; DETA/NO: green; Wash-out: orange) for the 3 clusters (clusters 1-3 from top to bottom). All tested conditions were not significant; Two-sided T-test. (**e**) Left: tRF kernels of the three conditions (Ctrl: black; DETA/NO: green; Wash-out: orange) for the 3 clusters (clusters 1-3 from top to bottom). Right: Full width at half minimum (FWHM) of the temporal RF kernels of the three conditions (Ctrl: black; DETA/NO: green; Wash-out: orange) for the 3 clusters. *: p<0.05; **: p<0.01, repeated measures ANOVA % Dunnett's test.

uli. Specifically, natural images or movies, stimuli that are closer to what the retina evolved to process (91), may be needed for a more complete picture of the functional implication of retinal neuromodulation. That natural stimuli can reveal novel nonlinear properties of retinal functions was demonstrated, for example, by Goldin et al. (87), who showed that an RGC's contrast selectivity can be context-dependent. Similarly, Höfling et al. (92) recorded natural movie-evoked RGC responses to train a convolutional neural network, which through *in silico* experiments allowed them to discover that transient suppressed-by-contrast RGC (G_{28}) feature center color-opponent responses and may signal context changes. These studies highlight that future studies on retinal neuromodulators should also employ natural stimuli.

Another important aspect to consider when studying NO neuromodulation in the retina is the level of light adaptation. Several studies proposed that NO facilitates the transition across light levels (66, 68, 69), especially to photopic conditions (36). Since we employed two-photon imaging, which inevitably results in a certain level of background 'illumination' (see discussion in (76, 93)), our experiments were performed in the low photopic range. Therefore, NO-mediated neuromodulation may serve additional light-level dependent functions: more globally during the transition from scotopic to mesopic/photopic, and more cell type-specific in the photopic regime – as we reported here.

Adaptational, cell type-specific response changes. Every recording method introduces technique-specific biases that have to be considered in the data analysis and interpretation. For two-photon imaging with fluorescent Ca^{2+} sensors, these potential biases include Ca^{2+} buffering, sensor bleaching by the excitation laser, and, in the case of bulk-loading with synthetic dyes (as in our experiments; see also (94)), slow leakage of the indicator from the cells. In retinal imaging, additional potentially confounding factors are an excitation laser-induced baseline activity and photoreceptor bleaching (77, 93). These biases are expected to be systematic, e.g., causing a decrease in signal-to-noise ratio across (RGC) responses (i.e., run-down). To account for this, we established a recording paradigm that produced a control and a NO-dataset consisting of paired RGC responses.

When analyzing the control dataset, we were surprised by finding response changes between both control measurements in approximately a third of the RGC types in the absence of the NO donor. These changes were consistent for a particular type but differed between types. Typically, we did not observe a simple overall decrease or increase in activity, but rather selective changes of response features: For instance, in G_{24} ('Slow On') only its response to high frequency and low contrast was reduced, while the remaining response features were not affected. Together, this strongly argues against a systematic, recording technique-related bias but rather for an adaptational effect. Currently, we can only speculate about the mechanism(s) underlying this type-specific adaptation. The most parsimonious explanation may be related to the *ex vivo* condition of the retina: While we allowed the tissue to settle and adapt to perfusion medium, light level, temperature, etc. for ∼25 min, extracellular signaling molecules, such as neuromodulators, may be depleted and washed out throughout the experiment,

resulting in differential adaptation of various RGC types. In any case, as type-selective adaptations can confound the recorded responses in a complex manner, a paired recording paradigm as the one described here, is recommended – in particular for pharmacological experiments.

Combining large-scale population recordings, RGC classification, and paired recordings to study neuromodulation of retinal output. In this study, we investigated the neuromodulatory effects of NO on the retinal output signal. To this end, we combined experimental and computational approaches to dissect NO-mediated effects at the RGC type-level. The latter is important for understanding neuromodulator function for early vision because the visual information is sent to the brain via parallel feature channels, represented by >40 RGC types in the mouse retina (5, 6, 85, 95). We demonstrated that our approach enabled us to distinguish adaptational from actual NO-induced effects using a rather simple and straightforward linear analysis (i.e., focusing on mean trace or RF size differences), which means that we may have missed potential nonlinear effects. The combination of two-photon Ca^{2+} imaging and MEA recordings allowed us to confirm our findings and make use of two methods that complement one another. Finally, the presented pipeline for analyzing neuromodulation in neural circuits constitutes a framework that can be easily extended by applying more advanced analyses.

ACKNOWLEDGEMENTS
We thank Gordon Eske & Merle Harrer for technical support and Clint L. Makino, Philipp Berens & Robert Feil for fruitful discussions. This work was funded by the Deutsche Forschungsgemeinschaft (DFG, German Research Foundation) 335549539/GRK2381 and CRC 1233 (project number 276693517). M. Goldin was funded by a fellowship from Fondation de France and by CNRS and by grant ANR PerBaCo.

Bibliography

1. Heinz Wassle and Brian B Boycott. Functional architecture of the mammalian retina. *Physiological reviews*, 71(2):447–480, 1991.
2. Richard H Masland. The fundamental plan of the retina. *Nature neuroscience*, 4(9): 877–886, 2001.
3. Heinz Wässle. Parallel processing in the mammalian retina. *Nature Reviews Neuroscience*, 5(10):747–757, 2004.
4. Tania A Seabrook, Timothy J Burbridge, Michael C Crair, and Andrew D Huberman. Architecture, function, and assembly of the mouse visual system. *Annual review of neuroscience*, 40:499–538, 2017.
5. Tom Baden, Philipp Berens, Katrin Franke, Miroslav Román Rosón, Matthias Bethge, and Thomas Euler. The functional diversity of retinal ganglion cells in the mouse. *Nature*, 529:345–350, 2016. ISSN 9781137332875. doi: 10.1038/nature16468.
6. J. Goetz, Z. F. Jessen, A. Jacobi, A. Mani, S. Cooler, D. Greer, S. Kadri, J. Segal, K. Shekhar, J. R. Sanes, and G. W. Schwartz. Unified classification of mouse retinal ganglion cells using function, morphology, and gene expression. *Cell Rep*, 40(2):111040, 2022. ISSN 2211-1247 (Electronic). doi: 10.1016/j.celrep.2022.111040.
7. James R Anderson, Bryan W Jones, Carl B Watt, Margaret V Shaw, Jia-Hui Yang, David DeMill, James S Lauritzen, Yanhua Lin, Kevin D Rapp, David Mastronarde, et al. Exploring the retinal connectome. *Molecular vision*, 17:355, 2011.
8. Robert E Marc, Bryan W Jones, Carl B Watt, James R Anderson, Crystal Sigulinsky, and Scott Lauritzen. Retinal connectomics: towards complete, accurate networks. *Progress in retinal and eye research*, 37:141–162, 2013.
9. Moritz Helmstaedter, Kevin L Briggman, Srinivas C Turaga, Viren Jain, H Sebastian Seung, and Winfried Denk. Connectomic reconstruction of the inner plexiform layer in the mouse retina. *Nature*, 500(7461):168–174, 2013.
10. Moritz Helmstaedter. Cellular-resolution connectomics: challenges of dense neural circuit reconstruction. *Nature methods*, 10(6):501–507, 2013.
11. Felice A Dunn and Rachel OL Wong. Wiring patterns in the mouse retina: collecting evidence across the connectome, physiology and light microscopy. *The Journal of physiology*, 592(22):4809–4823, 2014.
12. Jamie Johnston and Leon Lagnado. General features of the retinal connectome determine the computation of motion anticipation. *Elife*, 4:e06250, 2015.
13. Kevin L Briggman, Moritz Helmstaedter, and Winfried Denk. Wiring specificity in the direction-selectivity circuit of the retina. *Nature*, 471(7337):183–188, 2011.
14. Huayu Ding, Robert G Smith, Alon Poleg-Polsky, Jeffrey S Diamond, and Kevin L Briggman. Species-specific wiring for direction selectivity in the mammalian retina. *Nature*, 535(7610):105–110, 2016.
15. Paul Witkovsky. Dopamine and retinal function. *Documenta ophthalmologica*, 108:17–39, 2004.
16. Suva Roy and Greg D Field. Dopaminergic modulation of retinal processing from starlight to sunlight. *Journal of pharmacological sciences*, 140(1):86–93, 2019.
17. Rebekah A Warwick, Serena Riccitelli, Alina S Heukamp, Hadar Yaakov, Lea Ankri, Jonathan Mayzel, Noa Gilead, Reut Parness-Yossifon, and Michal Rivlin-Etzion. Top-down modulation of the retinal code via histaminergic neurons of the hypothalamus. *bioRxiv*, pages 2022–04, 2022.
18. Ursula Greferath, M Kambourakis, Christian Barth, EL Fletcher, and M Murphy. Characterization of histamine projections and their potential cellular targets in the mouse retina. *Neuroscience*, 158(2):932–944, 2009.
19. Justine Masson. Serotonin in retina. *Biochimie*, 161:51–55, 2019.
20. Stephen Yazulla. Endocannabinoids in the retina: from marijuana to neuroprotection. *Progress in retinal and eye research*, 27(5):501–526, 2008.
21. Thomas Schwitzer, Raymund Schwan, Karine Angioi-Duprez, Anne Giersch, and Vincent Laprevote. The endocannabinoid system in the retina: from physiology to practical and therapeutic applications. *Neural plasticity*, 2016, 2016.
22. Charles F Yates, Jin Y Huang, and Dario A Protti. Tonic endocannabinoid levels modulate retinal signaling. *International Journal of Environmental Research and Public Health*, 19 (19):12460, 2022.
23. Ira M Goldstein, Philipp Ostwald, and Steven Roth. Nitric oxide: a review of its role in retinal function and disease. *Vision research*, 36(18):2979–2994, 1996.
24. Alex H Vielma, Mauricio A Retamal, and Oliver Schmachtenberg. Nitric oxide signaling in the retina: what have we learned in two decades? *Brain research*, 1430:112–125, 2012.
25. Ana Santos-Carvalho, Ana Rita Alvaro, Joao Martins, Antonio Francisco Ambrosio, and Claudia Cavadas. Emerging novel roles of neuropeptide y in the retina: from neuromodulation to neuroprotection. *Progress in neurobiology*, 112:70–79, 2014.
26. Ana Santos-Carvalho, António Francisco Ambrósio, and Cláudia Cavadas. Neuropeptide y system in the retina: From localization to function. *Progress in retinal and eye research*, 47:19–37, 2015.
27. Wenjun Yan, Mallory A Laboulaye, Nicholas M Tran, Irene E Whitney, Inbal Benhar, and Joshua R Sanes. Mouse retinal cell atlas: molecular identification of over sixty amacrine cell types. *Journal of Neuroscience*, 40(27):5177–5195, 2020.
28. Matthew J Gastinger, Ning Tian, Tamas Horvath, and David W Marshak. Retinopetal axons in mammals: emphasis on histamine and serotonin. *Current eye research*, 31 (7-8):655–667, 2006.
29. Donald M O'Malley and Richard H Masland. Co-release of acetylcholine and gamma-aminobutyric acid by a retinal neuron. *Proceedings of the National Academy of Sciences*, 86(9):3414–3418, 1989.
30. Donald M O'Malley, Julie H Sandell, and Richard H Masland. Co-release of acetylcholine and gaba by the starburst amacrine cells. *Journal of Neuroscience*, 12(4):1394–1408, 1992.
31. Hajime Hirasawa, Rebecca A Betensky, and Elio Raviola. Corelease of dopamine and gaba by a retinal dopaminergic neuron. *Journal of Neuroscience*, 32(38):13281–13291, 2012.
32. Jeffrey S Diamond. Inhibitory interneurons in the retina: types, circuitry, and function. *Annual review of vision science*, 3:1–24, 2017.
33. Michael D Flood, Johnnie M Moore-Dotson, and Erika D Eggers. Dopamine d1 receptor activation contributes to light-adapted changes in retinal inhibition to rod bipolar cells. *Journal of neurophysiology*, 120(2):867–879, 2018.
34. Manvi Goel and Stuart C Mangel. Dopamine-mediated circadian and light/dark-adaptive modulation of chemical and electrical synapses in the outer retina. *Frontiers in Cellular Neuroscience*, 15:647541, 2021.
35. Rolf Herrmann, Stephanie J Heflin, Timothy Hammond, Bowa Lee, Jing Wang, Raul R Gainetdinov, Marc G Caron, Erika D Eggers, Laura J Frishman, Maureen A McCall, et al. Rod vision is controlled by dopamine-dependent sensitization of rod bipolar cells by gaba. *Neuron*, 72(1):101–110, 2011.
36. Jason Jacoby, Amurta Nath, Zachary F Jessen, and Gregory W Schwartz. A self-regulating gap junction network of amacrine cells controls nitric oxide release in the retina. *Neuron*, 100(5):1149–1162, 2018.
37. B Bauer, B Ehinger, and L Åberg. [3 h]-dopamine release from the rabbit retina. *Albrecht von Graefes Archiv für klinische und experimentelle Ophthalmologie*, 215:71–78, 1980.
38. Bernard F Godley and Richard J Wurtman. Release of endogenous dopamine from the superfused rabbit retina in vitro: effect of light stimulation. *Brain research*, 452(1-2): 393–395, 1988.
39. MBA Djamgoz and H-J Wagner. Localization and function of dopamine in the adult vertebrate retina. *Neurochemistry international*, 20(2):139–191, 1992.
40. Víctor Pérez-Fernández, Nina Milosavljevic, Annette E Allen, Kirstan A Vessey, Andrew I Jobling, Erica L Fletcher, Paul P Breen, John W Morley, and Morven A Cameron. Rod photoreceptor activation alone defines the release of dopamine in the retina. *Current Biology*, 29(5):763–774, 2019.
41. Charles W Nichols, David Jacobowitz, and Marianne Hottenstein. The influence of light and dark on the catecholamine content of the retina and choroid. *Investigative Ophthalmology & Visual Science*, 6(6):642–646, 1967.
42. Izhak Nir, Rashidul Haque, and P Michael Iuvone. Diurnal metabolism of dopamine in the mouse retina. *Brain research*, 870(1-2):118–125, 2000.
43. Christophe Ribelayga, Yu Cao, and Stuart C Mangel. The circadian clock in the retina controls rod-cone coupling. *Neuron*, 59(5):790–801, 2008.
44. W Wade Kothmann, Stephen C Massey, and John O'Brien. Dopamine-stimulated dephosphorylation of connexin 36 mediates aii amacrine cell uncoupling. *Journal of Neuroscience*, 29(47):14903–14911, 2009.

45. Nan Ge Jin and Christophe P Ribelayga. Direct evidence for daily plasticity of electrical coupling between rod photoreceptors in the mammalian retina. *Journal of Neuroscience*, 36(1):178–184, 2016.
46. Eric M Lasater and John E Dowling. Dopamine decreases conductance of the electrical junctions between cultured retinal horizontal cells. *Proceedings of the National Academy of Sciences*, 82(9):3025–3029, 1985.
47. Yuki Hayashida, Carolina Varela Rodríguez, Genki Ogata, Gloria J Partida, Hanako Oi, Tyler W Stradleigh, Sherwin C Lee, Anselmo Felipe Colado, and Andrew T Ishida. Inhibition of adult rat retinal ganglion cells by d1-type dopamine receptor activation. *Journal of Neuroscience*, 29(47):15001–15016, 2009.
48. Rebekah A Warwick, Alina S Heukamp, Serena Riccitelli, and Michal Rivlin-Etzion. Dopamine differentially affects retinal circuits to shape the retinal code. *The Journal of physiology*, 2023.
49. David S Bredt, Paul M Hwang, and Solomon H Snyder. Localization of nitric oxide synthase indicating a neural role for nitric oxide. *Nature*, 347(6295):768–770, 1990.
50. Ted M Dawson, David S Bredt, Majid Fotuhi, Paul M Hwang, and Solomon H Snyder. Nitric oxide synthase and neuronal nadph diaphorase are identical in brain and peripheral tissues. *Proceedings of the National Academy of Sciences*, 88(17):7797–7801, 1991.
51. R Yamamoto, DS Bredt, SH Snyder, and RA Stone. The localization of nitric oxide synthase in the rat eye and related cranial ganglia. *Neuroscience*, 54(1):189–200, 1993.
52. Ryo Yamamoto, David S Bredt, Ted M Dawson, Solomon H Snyder, and Richard A Stone. Enhanced expression of nitric oxide synthase by rat retina following pterygopalatine parasympathetic denervation. *Brain research*, 631(1):83–88, 1993.
53. Todd A Blute, Bernd Mayer, and William D Eldred. Immunocytochemical and histochemical localization of nitric oxide synthase in the turtle retina. *Visual Neuroscience*, 14(4): 717–729, 1997.
54. Todd A Blute, Michael R Lee, and William D Eldred. Direct imaging of nmda-stimulated nitric oxide production in the retina. *Visual Neuroscience*, 17(4):557–566, 2000.
55. William D Eldred and Todd A Blute. Imaging of nitric oxide in the retina. *Vision research*, 45(28):3469–3486, 2005.
56. Vikram Palamalai, Ruth M Darrow, Daniel T Organisciak, and Masaru Miyagi. Light-induced changes in protein nitration in photoreceptor rod outer segments. *Mol Vis*, 12: 1543–1551, 2006.
57. Jan J Blom, Todd A Blute, and William D Eldred. Functional localization of the nitric oxide/cgmp pathway in the salamander retina. *Visual Neuroscience*, 26(3):275–286, 2009.
58. Silke Haverkamp and Heinz Wässle. Immunocytochemical analysis of the mouse retina. *Journal of Comparative Neurology*, 424(1):1–23, 2000.
59. Thomas J Giove, Monika M Deshpande, and William D Eldred. Identification of alternate transcripts of neuronal nitric oxide synthase in the mouse retina. *Journal of neuroscience research*, 87(14):3134–3142, 2009.
60. Jan J Blom, Tom Giove, Monika Deshpande, and William D Eldred. Characterization of nitric oxide signaling pathways in the mouse retina. *Journal of Comparative Neurology*, 520(18):4204–4217, 2012.
61. Gerard P Ahern, Vitaly A Klyachko, and Meyer B Jackson. cgmp and s-nitrosylation: two routes for modulation of neuronal excitability by no. *Trends in neurosciences*, 25(10): 510–517, 2002.
62. Ari Sitaramayya. Soluble guanylate cyclases in the retina. *Molecular and cellular biochemistry*, 230:177–186, 2002.
63. John Garthwaite. Dynamics of cellular no-cgmp signaling. *Frontiers in Bioscience-Landmark*, 10(2):1868–1880, 2005.
64. Masaru Miyagi, Hirokazu Sakaguchi, Ruth M Darrow, Lin Yan, Karen A West, Kulwant S Aulak, Dennis J Stuehr, Joe G Hollyfield, Daniel T Organisciak, and John W Crabb. Evidence that light modulates protein nitration in rat retina. *Molecular & Cellular Proteomics*, 1(4):293–303, 2002.
65. Douglas T Hess, Akio Matsumoto, Sung-Oog Kim, Harvey E Marshall, and Jonathan S Stamler. Protein s-nitrosylation: purview and parameters. *Nature reviews Molecular cell biology*, 6(2):150–166, 2005.
66. Stephen L Mills and Stephen C Massey. Differential properties of two gap junctional pathways made by aii amacrine cells. *Nature*, 377(6551):734–737, 1995.
67. Scott Nawy and Craig E Jahr. Suppression by glutamate of cgmp-activated conductance in retinal bipolar cells. *Nature*, 346(6281):269–271, 1990.
68. Josefin Snellman and Scott Nawy. cgmp-dependent kinase regulates response sensitivity of the mouse on bipolar cell. *Journal of Neuroscience*, 24(29):6621–6628, 2004.
69. Ryan E Tooker, Mikhail Y Lipin, Valerie Leuranguer, Eva Rozsa, Jayne R Bramley, Jacqueline L Harding, Melissa M Reynolds, and Jozsef Vigh. Nitric oxide mediates activity-dependent plasticity of retinal bipolar cell output via s-nitrosylation. *Journal of Neuroscience*, 33(49):19176–19193, 2013.
70. Alex H Vielma, Adolfo Agurto, Joaquín Valdés, Adrián G Palacios, and Oliver Schmachtenberg. Nitric oxide modulates the temporal properties of the glutamate response in type 4 off bipolar cells. *PLoS One*, 9(12):e114330, 2014.
71. Guo-Yong Wang, Lauren C Liets, and Leo M Chalupa. Nitric oxide differentially modulates on and off responses of retinal ganglion cells. *Journal of neurophysiology*, 90(2): 1304–1313, 2003.
72. Guo-Yong Wang, Deborah A Van der List, Joseph P Nemargut, Julie L Coombs, and Leo M Chalupa. The sensitivity of light-evoked responses of retinal ganglion cells is decreased in nitric oxide synthase gene knockout mice. *Journal of Vision*, 7(14):7–7, 2007.
73. Joseph P Nemargut and Guo-Yong Wang. Inhibition of nitric oxide synthase desensitizes retinal ganglion cells to light by diminishing their excitatory synaptic currents under light adaptation. *Vision research*, 49(24):2936–2947, 2009.
74. Iqbal Ahmad, Trese Leinders-Zufall, Jeffery D Kocsis, Gordon M Shepherd, Frank Zufall, and Colin J Barnstable. Retinal ganglion cells express a cgmp-gated cation conductance activatable by nitric oxide donors. *Neuron*, 12(1):155–165, 1994.
75. Fusao Kawai and Peter Sterling. cgmp modulates spike responses of retinal ganglion cells via a cgmp-gated current. *Visual neuroscience*, 19(3):373–380, 2002.
76. Thomas Euler, Susanne E. Hausselt, David J. Margolis, Tobias Breuninger, Xavier Castell, Peter B. Detwiler, and Winfried Denk. Eyecup scope—optical recordings of light stimulus-evoked fluorescence signals in the retina. *Pflügers Archiv - European Journal of Physiology*, 457:1393–1414, 2009. doi: 10.1007/s00424-008-0603-5.
77. Thomas Euler, Katrin Franke, and Tom Baden. Studying a light sensor with light: Multiphoton imaging in the retina. e. hartveit (ed.). *Multiphoton Microscopy, Neuromethods (Humana, New York, NY)*, 148:225–250, 2019. doi: 10.1007/978-1-4939-9702-2_10.
78. Zhijian Zhao, David A Klindt, André Maia Chagas, Klaudia P Szatko, Luke Rogerson, Dario A Protti, Christian Behrens, Deniz Dalkara, Timm Schubert, Matthias Bethge, et al. The temporal structure of the inner retina at a single glance. *Scientific reports*, 10(1):1–17, 2020.
79. Dominic Gonschorek, Larissa Höfling, Klaudia P Szatko, Katrin Franke, Timm Schubert, Benjamin Dunn, Philipp Berens, David Klindt, and Thomas Euler. Removing inter-experimental variability from functional data in systems neuroscience. *Advances in Neural Information Processing Systems*, 34:3706–3719, 2021.
80. Yongrong Qiu, David A. Klindt, Klaudia P. Szatko, Dominic Gonschorek, Larissa Hoefling, Timm Schubert, Laura Busse, Matthias Bethge, and Thomas Euler. Efficient coding of natural scenes improves neural system identification. *bioRxiv*, page 2022.01.10.475663, 2022. doi: 10.1101/2022.01.10.475663.
81. J Weiss, GA O'sullivan, L Heinze, H-X Chen, H Betz, and H Wässle. Glycinergic input of small-field amacrine cells in the retinas of wildtype and glycine receptor deficient mice. *Molecular and Cellular Neuroscience*, 37(1):40–55, 2008.
82. F Muller, H Wassle, and Th Voigt. Pharmacological modulation of the rod pathway in the cat retina. *Journal of neurophysiology*, 59(6):1657–1672, 1988.
83. Ilya Buldyrev, Theresa Puthussery, and W Rowland Taylor. Synaptic pathways that shape the excitatory drive in an off retinal ganglion cell. *Journal of neurophysiology*, 107(7): 1795–1807, 2012.
84. Amanda J McLaughlin, Kumiko A Percival, Jacqueline Gayet-Primo, and Teresa Puthussery. Glycinergic inhibition targets specific off cone bipolar cells in primate retina. *Eneuro*, 8(1), 2021.
85. J Alexander Bae, Shang Mu, Jinseop S Kim, Nicholas L Turner, Ignacio Tartavull, Nico Kemnitz, Chris S Jordan, Alex D Norton, William M Silversmith, Rachel Prentki, et al. Digital museum of retinal ganglion cells with dense anatomy and physiology. *Cell*, 173 (5):1293–1306, 2018.
86. EJ Chichilnisky. A simple white noise analysis of neuronal light responses. *Network: computation in neural systems*, 12(2):199, 2001.
87. Matías A Goldin, Baptiste Lefebvre, Samuele Virgili, Mathieu Kim Pham Van Cang, Alexander Ecker, Thierry Mora, Ulisse Ferrari, and Olivier Marre. Context-dependent selectivity to natural images in the retina. *Nature Communications*, 13(1):5556, 2022.
88. Francesco Trapani, Giulia Lia Beatrice Spampinato, Pierre Yger, and Olivier Marre. Differences in nonlinearities determine retinal cell types. *Journal of Neurophysiology*, 130 (3):706–718, 2023.
89. Todd A Blute, Paula Velasco, and William D Eldred. Functional localization of soluble guanylate cyclase in turtle retina: modulation of cgmp by nitric oxide donors. *Visual neuroscience*, 15(3):485–498, 1998.
90. Sebastian Gotzes, Jan de Vente, and Frank Mueller. Nitric oxide modulates cgmp levels in neurons of the inner and outer retina in opposite ways. *Visual neuroscience*, 15(5): 945–955, 1998.
91. Yongrong Qiu, Zhijian Zhao, David Klindt, Magdalena Kautzky, Klaudia P Szatko, Frank Schaeffel, Katharina Rifai, Katrin Franke, Laura Busse, and Thomas Euler. Natural environment statistics in the upper and lower visual field are reflected in mouse retinal specializations. *Current Biology*, 31(15):3233–3247, 2021.
92. Larissa Höfling, Klaudia P Szatko, Christian Behrens, Yongrong Qiu, David Alexander Klindt, Zachary Jessen, Gregory S Schwartz, Matthias Bethge, Philipp Berens, Katrin Franke, et al. A chromatic feature detector in the retina signals visual context changes. *bioRxiv*, pages 2022–11, 2022.
93. Thomas Euler, Susanne E Hausselt, David J Margolis, Tobias Breuninger, Xavier Castell, Peter B Detwiler, and Winfried Denk. Eyecup scope—optical recordings of light stimulus-evoked fluorescence signals in the retina. *Pflügers Archiv-European Journal of Physiology*, 457:1393–1414, 2009.
94. Kevin L Briggman and Thomas Euler. Bulk electroporation and population calcium imaging in the adult mammalian retina. *Journal of neurophysiology*, 105(5):2601–2609, 2011.
95. Nicholas M Tran, Karthik Shekhar, Irene E Whitney, Anne Jacobi, Inbal Benhar, Guosong Hong, Wenjun Yan, Xian Adiconis, McKinzie E Arnold, Jung Min Lee, et al. Single-cell profiles of retinal ganglion cells differing in resilience to injury reveal neuroprotective genes. *Neuron*, 104(6):1039–1055, 2019.
96. Katrin Franke, André Maia Chagas, Zhijian Zhao, Maxime JY Zimmermann, Philipp Bartel, Yongrong Qiu, Klaudia P Szatko, Tom Baden, and Thomas Euler. An arbitrary-spectrum spatial visual stimulator for vision research. *elife*, 8:e48779, 2019.
97. Klaudia P Szatko, Maria M Korympidou, Yanli Ran, Philipp Berens, Deniz Dalkara, Timm Schubert, Thomas Euler, and Katrin Franke. Neural circuits in the mouse retina support color vision in the upper visual field. *Nature communications*, 11(1):3481, 2020.
98. Pierre Yger, Giulia LB Spampinato, Elric Esposito, Baptiste Lefebvre, Stéphane Deny, Christophe Gardella, Marcel Stimberg, Florian Jetter, Guenther Zeck, Serge Picaud, et al. A spike sorting toolbox for up to thousands of electrodes validated with ground truth recordings in vitro and in vivo. *Elife*, 7:e34518, 2018.
99. Olivier Marre, Dario Amodei, Nikhil Deshmukh, Kolia Sadeghi, Frederick Soo, Timothy E Holy, and Michael J Berry. Mapping a complete neural population in the retina. *Journal of Neuroscience*, 32(43):14859–14873, 2012.
100. William H Press and Saul A Teukolsky. Savitzky-golay smoothing filters. *Computers in Physics*, 4(6):669–672, 1990.
101. Pauli Virtanen, Ralf Gommers, Travis E. Oliphant, Matt Haberland, Tyler Reddy, David Cournapeau, Evgeni Burovski, Pearu Peterson, Warren Weckesser, Jonathan Bright, Stéfan J. van der Walt, Matthew Brett, Joshua Wilson, K. Jarrod Millman, Nikolay Mayorov, Andrew R. J. Nelson, Eric Jones, Robert Kern, Eric Larson, C J Carey, İlhan Polat, Yu Feng, Eric W. Moore, Jake VanderPlas, Denis Laxalde, Josef Perktold, Robert Cim-

rman, Ian Henriksen, E. A. Quintero, Charles R. Harris, Anne M. Archibald, Antônio H. Ribeiro, Fabian Pedregosa, Paul van Mulbregt, and SciPy 1.0 Contributors. SciPy 1.0: Fundamental Algorithms for Scientific Computing in Python. *Nature Methods*, 17:261–272, 2020. doi: 10.1038/s41592-019-0686-2.

102. Ziwei Huang, Yanli Ran, Jonathan Oesterle, Thomas Euler, and Philipp Berens. Estimating smooth and sparse neural receptive fields with a flexible spline basis. *arXiv preprint arXiv:2108.07537*, 2021.

103. Adrian M Price-Whelan, BM Sipőcz, HM Günther, PL Lim, SM Crawford, S Conseil, DL Shupe, MW Craig, N Dencheva, A Ginsburg, et al. The astropy project: Building an open-science project and status of the v2. 0 core package. *The Astronomical Journal*, 156(3):123, 2018.

104. Hui Zou, Trevor Hastie, and Robert Tibshirani. Sparse principal component analysis. *Journal of computational and graphical statistics*, 15(2):265–286, 2006.

Methods

Animals and tissue preparation for two-photon Ca^{2+} imaging. All animals for the two-photon Ca^{2+} imaging experiments were conducted at the University of Tübingen and were performed according to the laws governing animal experimentation issued by the German Government as well as approved by the institutional animal welfare committee of the University of Tübingen. For all experiments, we used retinae (n=26) from C57Bl/6J mice (n=14; JAX 000664) of either sex between the age of 4-16 weeks. All animals were kept in the local animal facility and housed under the standard 12h/12h day/night cycle at 22°C and a humidity of 55%.

The following procedures were carried out under very dim red (> 650 nm) light. Before each imaging experiment, the animal was dark-adapted for >1h, then anesthetized with isoflurane (CP-Pharma) and sacrificed by cervical dislocation. Immediately after, the eyes were enucleated with a dorsal cut as orientation landmark and hemisected in carboxygenated (95% O_2, 5% CO_2) artificial cerebrospinal fluid (ACSF) solution containing (in mM): 125 NaCl, 2.5 KCl, 2 $CaCl_2$, 1 $MgCl_2$, 1.25 NaH_2PO_4, 26 $NaHCO_3$, 20 glucose, and 0.5 L-glutamine at pH 7.4. Sulforhodamine-101 (SR101, 0.1 µM; Invitrogen) was added to the ACSF to reveal blood vessels and damaged ganglion cell layer (GCL) cells in the red fluorescence channel (76). The carboxygenated ACSF was constantly perfused through the recording chamber at 4 ml/min and kept at ∼36°C throughout the entire experiment. After the dissection, retinae were bulk-electroporated with the synthetic fluorescent calcium indicator Oregon-Green 488 BAPTA-1 (OGB-1; hexapotassium salt; Life Technologies) (94). To electroporate the GCL, the dissected retina was flat-mounted with the GCL facing up onto an AnodiscTM (#13, 0.1 µm pore size, 13 mm diameter, Cytiva), and then placed between two 4 mm horizontal platinum disk electrodes (CUY700P4E/L, Nepagene/Xceltis). The lower electrode was covered with 15 µl of ACSF, while a 10 µl drop of 5 mM OGB-1 dissolved in ACSF was suspended from the upper electrode and lowered onto the retina. Then, nine electrical pulses (∼9.2 V, 100 ms pulse width, at 1 Hz) from a pulse generator/wide-band amplifier combination (TGP110 and WA301, Thurlby handar/Farnell) were applied and then, the electroporated retina on the Anodisc was transferred into the recording chamber, whereby the dorsal edge of the retina pointed away from the experimenter. The retina was left there for ∼30 min to recover, as well as adapted to the light stimulation by displaying a binary dense noise stimulus (20 x 15 matrix, 40 x 40 μm^2 pixels, balanced random sequence) at 5 Hz before the recordings started.

Two-photon Ca^{2+} imaging. For the functional Ca^{2+} imaging experiments, a MOM-type two-photon microscope (designed by W. Denk, MPI, Heidelberg; purchased from Sutter Instruments/Science Products) (76, 77) was employed. The microscope was equipped with a mode-locked Ti:Sapphire laser (MaiTai-HP DeepSee, Newport Spectra-

Physics) tuned to 927 nm (ideal wavelength to excite OGB-1), two photomultiplier tubes serving as fluorescence detection channels for OGB-1 (HQ 510/84, AHF/Chroma) and SR101 (HQ 630/60, AHF), and a water immersion objective (CF175 LWD×16/0.8W, DIC N2, Nikon, Germany). To acquire images, custom-made software (ScanM by M. Müller and T. Euler) running under IGOR Pro 6.3 for the operating system Microsoft Windows (Wavemetrics) was used and time-lapsed 64 x 64 pixel image scans ($\sim$100 µm^2) at 7.8125 Hz were taken. Routinely, the optic nerve position and the scan field position were recorded to reconstruct their retinal positions. High-resolution images (512 x 512 pixel images) were recorded to support semi-automatic ROI detection.

Light stimulation for two-photon Ca^{2+} imaging. For the light stimulation of the retinal tissue, a digital light processing (DLP) projector (lightcrafter (LCr), DPM-E4500UVBGMKII, EKB Technologies Ltd) was used to display the visual stimuli through the objective onto the retina, whereby the stimulus was focused on the photoreceptor layer (96). The LCr was equipped with a light-guide port to couple in external, band-pass filtered green and UV light-emitting diode (LEDs; green: 576 BP 10, F37-576; UV: 387 BP 11, F39-387; both AHF/Chroma). The band-pass filter was used to optimize the spectral separation of mouse M- and S- opsins (390/576 Dualband, F59-003, AHF/Chroma). Both LEDs were synchronized with the scan retracing of the microscope. Stimulator intensity (as photoisomerization rate, 10^3 P*s^{-1} per cone) was calibrated to range from $\sim$0.5 (black image) to $\sim$20 for M- and S-opsins, respectively. Steady illumination of $\sim 10^4$ P*s^{-1} per cone was present during the scan recordings due to the two-photon excitation of photopigments (76, 77).

In total, three types of light stimuli were used for the imaging of Ca^{2+} in the GCL: (1) full-field chirp stimulus (700 µm ⌀; see details here ref. (5)), (2) bright moving bar (0.3 x 1 mm) at 1 mm s^{-1} in eight directions to probe direction and orientation selectivity, and (3) random binary noise with a checkerboard grid of 20 x 15 checks and a check size of 40 µm at 5 Hz for 5 min to map receptive fields. Before each stimulus was presented, the baseline was recorded after the laser started scanning for at least 30 s to avoid immediate laser-induced effects on the retinal activity (76, 77, 97).

Animals and tissue preparation for electrophysiological recordings. Electrophysiological data were recorded from isolated retinae from four C57Bl/6J mice of 8 - 10 weeks. The experiment was performed in accordance with the institutional animal care standards of Sorbonne Université. (Paris, France). The animals were housed in enriched cages with ad libitum food, and watering. The ambient temperature was between 22 and 25°C, the humidity was between 50 and 70%, and the light cycle was 12–14h of light, 10–12h of darkness. After killing the animal, the eye was enucleated and transferred rapidly into oxygenated Ames medium (Sigma-Aldrich). Dissection was made under dim light condition as described previously (98, 99).

Electrophysiological recordings. For the electrophysiological recordings, we mounted a piece of retina onto a membrane and then lowered it with the ganglion cell side against a 252-channel multi-electrode array (MEA) whose electrodes were spaced by 30 µm. During dissection and recordings, the tissue was perfused with oxygenated Ames solution and a peristaltic perfusion system with two independent pumps: PPS2 (Multichannel Systems GmbH). Mice retinae were kept at 35–37°C during the whole experiment. The data sampling rate was 20 kHz. The raw signal was acquired through MC Rack Multi-channel Systems software 4.6.2, it was high-pass filtered at 100 Hz, and the spikes were isolated using SpyKING CIRCUS 1.0.628 (98). Subsequent data analysis was done with custom-written Python codes. We extracted the activity of a total of 391 neurons. We kept cells with a low number of refractory period violations (< 0.95%, with median < 0.05% for all experiments, 2 ms refractory period) and whose template waveform could be well distinguished from the template waveforms of other cells. These constraints ensured a good quality of the reconstructed spike trains. In addition, we discarded neurons that showed no or almost no responses to chirp stimulus, preventing the correct cell classification.

Light stimulation for electrophysiological recordings. A white-mounted LED (MCWHLP1, Thorlabs Inc.) was used as a light source, and the stimuli were displayed using a Digital Mirror Device (DLP9500, Texas Instruments) and focused on the photoreceptors using standard optics and an inverted microscope (Nikon). The light level corresponded to photopic vision: 4.9×10^4 and 1.4×10^5 isomerizations / (photoreceptor.s) for S-cones and M-cones, respectively. In total, we displayed two stimuli: *(1)* a random binary checkerboard with check size of 42 µm for 30-40 min at 30 Hz, and *(2)* a full field chirp stimulus as used for the two-photon Ca^{2+} imaging experiments. It was played at 50 Hz, containing 20 repetitions of 32 s length.

Pharmacology. All used drugs were added to the carboxygenated, perfused ACSF solution 15 min prior to the second recording of the GCL scan fields. For the drugs, the respective concentrations were used (in µM): 100 (Z)-1-[N-(2-aminoethyl)-N-(2-ammonioethyl)amino]diazen-1-ium-1,2-diolate (DETA/NO) and 1 strychnine. The ACSF solution with and without drug application was always kept at $\sim$36°C.

Data Analysis of two-photon Ca^{2+} imaging recordings. Image extraction and semi-automatic region-of-interest (ROI) detection were performed using Igor PRO 8. All analyses were organized and performed in a custom-written schema using DataJoint for Python http://datajoint.github.io/; D. Yatsenko, Tolias lab, Baylor College of Medicine.

Preprocessing. After the Ca^{2+} were extracted from individual ROIs, as described elsewhere (5, 97), the raw traces were detrended by subtracting a smoothed version of the trace from the raw one. Detrending was necessary to remove slow drifts in the signal that were unrelated to the light-induced response. The smoothed version was the trace was computed by applying a Savitzky-Golay filter (100) of 3rd polynomial order and a window length of 60 s using the Python SciPy implementation $scipy.signal.savgol_filter$ (101).

$$r_{detrend} = r_{raw} - r_{smooth}$$

Lastly, the baseline activity (mean of the first eight samples) was subtracted, the mean activity $r(t)$ was computed and then traces were normalized such that:

$$\max_t(|r(t)|) = 1$$

Inclusion criterion. To include reliable cell responses for the performed analyses, two consecutive quality filtering steps were applied. At first, the response quality criterion, also termed quality index (QI), was computed for the moving bar ($QI_{MB} > 0.6$) and full-field chirp ($QI_{chirp} > 0.45$). Cells that passed either one of these two QIs in both recording conditions were included, otherwise they were discarded in the following analyses. As in Baden et al. (5), the quality index is defined as follows:

$$QI = \frac{Var[\langle C \rangle_r]_t}{\langle Var[C]_t \rangle_r}$$

where C is the T by R response matrix (time samples by stimulus repetitions) and $\langle\rangle_x$ and $Var[]_x$ denote the mean and variance across the indicated dimension x, respectively. As a second step, cells were assigned to an RGC group using the RGC classifier, which returned the RGC group index and a confidence score (i.e., assignment probability to the predicted RGC group by the random forest classifier (80)). Only cells that were assigned to one of the RGC groups (i.e., RGC index 1 - 32) were included, whereas cells assigned to a displaced AC group (i.e., RGC index 33 - 46) were rejected. Cells that exceeded the confidence score threshold of > 0.25 were included.

Suppression index. For each cell, the suppression index (SI) was measured by comparing the (absolute) negative area under the curve (AUC_{neg}) of the chirp and moving bar responses with the total area under the curve (AUC_{neg}+AUC_{pos}) of the entire response trace. For the absolute AUC_{neg}, the response was clipped for value <0.

$$SI = \frac{|AUC_{neg}|}{|AUC_{neg}| + |AUC_{pos}|}$$

Trace difference Δ. To compute the trace difference between the paired responses per cell, we subtracted the first response average to the chirp and moving bar stimuli, i.e., Ctrl 1, from the second recorded light-induced response, i.e., either NO or Ctrl 2. For the cell type-specific analysis, we computed the average trace differences per cell. For the feature-based analysis, we computed the average trace differences per feature and per cell type.

On-Off Index. The On-Off index was computed as

$$OOI = \frac{\langle r_{on} \rangle_t - \langle r_{off} \rangle_t}{\langle r_{on} \rangle_t + \langle r_{off} \rangle_t}$$

where r_{on} and r_{off} are defined as the separated time components of the moving bar response into its On- and Off-component. For each component, we computed the mean value of the discrete differences along the time axis clipped between 0 and 1 to estimate if there is a response to the particular feature.

Classification of functional retinal ganglion cell types. For the functional classification of RGC types, we used a previously published RGC classifier (80). The classifier, which uses a random forest classifier, was trained, validated, and tested on previously published RGC type responses (5). As input to the classifier, we used the responses to the standard set of stimuli, i.e., full-field chirp and moving bar, as well as soma sizes (separates alpha and non-alpha types) and the p-values of the permutation test for direction selectivity (separates DS and Non-DS types). For every cell, the RGC classifier outputs its type index and the confidence scores for all 46 types. The confidence score, as described in 'inclusion criterion' was used as a quality criterion.

Receptive field estimation. We mapped receptive fields (RFs) of RGCs using the RF python toolbox *RFEst* (102), following the procedure in (5) with few modifications. The binary dense noise stimulus (20 x 15 matrix, (40 µm)^2 pixels, balanced random sequence; 5 Hz) was centered on the recording field. We computed the temporal gradients of the Ca^{2+} signals from the detrended traces and clipped negative values:

$$\dot{c} = \max(0, \dot{r}_{detrend})$$

The stimulus $S(t)$ and the clipped temporal gradients c were upsampled to 10 times the stimulus frequency to compute the gradient-triggered average stimulus:

$$\boldsymbol{F}(x,y,\tau) = \int_{t=0}^{T} \dot{c}(t)\boldsymbol{S}(x,y,t+\tau)$$

where $\boldsymbol{S}(x,y,t)$ is the stimulus, τ is the lag ranging from approximately -0.20 to 1.38 seconds, and T is the duration of the stimulus. We smoothed these raw RF using a 5×5 pixel and 1 pixel standard deviation Gaussian window for each lag. Then we decomposed the RF into a temporal ($F_t(\tau)$) and spatial ($\boldsymbol{F}_s(x,y)$) component using singular value decomposition and scaled them such that $\max(|F_t|) = 1$ and $\max(|\boldsymbol{F}_s|) = \max(|\boldsymbol{F}|)$. RF quality was computed as:

$$QI_{\text{RF}} = 1 - \frac{Var[\boldsymbol{F}(x,y,\tau) - F_t(\tau)\boldsymbol{F}_s(x,y)]}{Var[\boldsymbol{F}(x,y,t)]}$$

Only RFs with $QI_{\text{RF}} > 0.45$ were used for the analysis.

For each spatial RF $\boldsymbol{F}_s$, we fit a 2D Difference of Gaussians using the python package *astropy* (103). The mean and covariance matrices of the center and surround Gaussian fits were tied, except for a linear scaling of the covariance matrix. We defined the polarity $p \in \{-1, 1\}$ of the spatial RF as the sign of the model fit at its mean. Next, we computed the center RF of the spatial RF as $\boldsymbol{F}_s^c = \max(0, p \cdot \boldsymbol{F}_s)$. The surround index was computed as:

$$RF_{surround} = \frac{\sum_{x,y}(\boldsymbol{F}_s - \boldsymbol{F}_s^c)}{\sum_{x,y}(|\boldsymbol{F}_s|)}.$$

To measure the center RF size, we fit a 2D Gaussian to the center RF, with the mean fixed to the one obtained from the Difference of Gaussians fit. The area covered by two standard deviations of this Gaussian fit was used as the RF size.

Functional clustering. The functional clustering was based on a similar approach as in (5). The clustering was only applied on RGC types previously classified as G_{32} and only recorded in Ctrl 1. First, visual features from the full-field chirp and moving bar Ca^{2+} responses were extracted using sparse principal component analysis (104). After optimizing the alpha parameter for each stimulus, each cell's dimensionality was reduced to 30 features, whereby the chirp covered 20 and the moving bar 10 features. Alpha was optimized in a way that every part of each stimulus was represented by one feature to increase interpretability. Each feature was standardized across cells before clustering. Then, the features were used to cluster the cells using a Mixture of Gaussian model. The ideal number of clusters was chosen based on the cross-validated Bayesian Information Criterion. Additionally, cluster coherence was computed and validated using intra- and inter-cluster correlation, as well as the influence of potential batch effects, i.e., a single cluster originates from a single retina or scan field, but is found across several ones. Then, the model was used to predict cell type labels. Finally, cluster 3 showed a high signal-to-noise ratio, thus cells were re-clustered, which originated in three clusters, whereby two showed high variability in their chirp and moving bar responses. These cells were discarded in the further analysis to clean this cluster from potential contamination.

Statistical analysis. To quantify the differences between traces, a Shaprio-Wilk test was used to test for normality and then either the two-sided t-test (if normally distributed) or the non-parametric Wilcoxon signed-rank test (Mann-Whitney U Test). To determine α, Bonferroni correction was used, depending on the number of tests performed. To test the difference between traces against zero, we either used the t-test or the non-parametric Wilcoxon signed-rank test, depending on the distribution. A one-sampled T-test was performed to test the mean against a population mean of zero to quantify if the mean difference diverges from zero. For the statistical comparison of the suppression index between conditions per cluster, the non-parametric Kruskal-Wallis one-way analysis of variance and post-hoc Dunnett's test and Bonferroni correction to determine the statistical significance between conditions were used.

Data Analysis of electrophysiological recordings.

Functional clustering. To cluster cells in different functional types, we based our analysis on the chirp and checkerboard stimulus responses and represented each RGC with a reduced vector. To obtain these vectors, first, we constructed peri-stimulus histograms (PSTH) from the spikes evoked from the chirp stimulus, using a binning of 100 ms, and spike-triggered averages (STA). Then, for each experiment, we z-scored all PSTHs and performed a principle component analysis (PCA) on them. We kept the number of components that were needed to explain 80% variance of the data (11-12 components for the PSTH). Second, we used the temporal profile (40 samples at 30 Hz) of each cell's STA obtained using the checkerboard stimulus. We z-scored it and performed a PCA, keeping two components, which explains around 80% of the variance. This adds information about the classical STA polarity of the RGCs. Third, we used the area of the ellipse fitted to the classical STA, as the product value of their major and minor axis σ values. These areas were normalized from 0 to 1. In this way, we obtain a data vector of around 15 values, depending on the experiment, that describes each RGC according to their response to a chirp and a checkerboard. Then, we performed an agglomerative clustering, setting the threshold value in a way that all clusters looked homogeneous across PSTHs and STAs. This resulted in over-clustering producing between 12 and 44 RGC groups (from 29 to 149 cells in each experiment).

Receptive field estimation. To estimate spatial and temporal receptive fields, we displayed a random binary checkerboard with check size of 42 µm for 30-40 min at 30 Hz. A three-dimensional spike-triggered average (STA; x, y, and time) was sampled using 40 time samples. The spatial STA presented across all the figures was obtained as the 2-dimensional spatial slice at the maximum value after smoothing. The temporal STA is the one-dimensional time slice at that same value. A double Gaussian fit was performed on the resulting spatial STA, and the ellipse corresponding to a 2σ contour of the fit was plotted for all the figures.

Pseudo-calcium transformation. In the last step, we assigned each cluster group to one of the 32 types described in Baden et al. (5). To do this, we used the Ca^{2+} imaging data to match it with the electrophysiological data. We based our analysis on their reported data in the Extended data from Fig. 1, where the authors link electrophysiology and Ca^{2+} imaging by means of a convolution between a Ca^{2+} event-triggered by a single spike. We transformed the PSTHs by convolving them with a decaying exponential (see Fig. 7c), in which we adjusted the temporal decay constant to maximize the correlation of the cluster groups and theirs (median maximum correlation of 0.78). RGC types that presented strong responses to the modulating frequencies and

amplitude were assigned correctly, while other types, which mostly respond to ON/OFF steps, were assigned in a second round of correlation match after excluding the former groups. Besides the correlation of the chirp traces, we confirmed the correct assigning of groups by checking that the ellipses of each type form a proper mosaic (see Fig. 7a,b), that the spatial STAs look uniform, and the similarity of their spike waveforms. After doing this for every experiment, we grouped the cells of each type across animals where we found a clear homogeneity. Finally, we computed a correlation matrix between the average chirp response of each type to show that the groups are homogeneous (see Fig. 7e).

Functional cell typing of G_{32}. Once we obtained all the cells assigned to G_{32}, we pooled the data from the 4 experiments and performed the same steps as before, to further distinguish sub-groups as we did with the Ca^{2+} imaging data. We first over-clustered again in this step and merged the similar sub-clusters in a last step. We obtained again, now in the electrophysiological data, three clearly differentiated subgroups. From an initial set of 46 cells, we obtained three subgroups of 17, 10, and 15 cells (Fig. 8c), plus a non-homogeneous subgroup of four cells that did not fit into any of them and was discarded.

Statistical analysis. To quantify the ellipses of the sRFs, we used the two-sides T-test. To quantify if the FWHM values of the tRFs were significantly different, we performed repeated measures ANOVA and post-hoc Dunnett's test. Only cells where we could compute sRFs or tRFs across the three conditions were used for these analyses.

Data and code availability. Data, light stimuli, as well as all custom analyses including code and notebooks to reproduce analyses will be made available at https://github.com/eulerlab upon journal publication.

Author contributions. D.G., Z.Z., T.E., and T.S. designed the study; T.S. wrote the animal protocol with the help of D.G. and T.E.; D.G. performed the imaging and electrophysiological experiments, supported by M.A.G., R.A., and T.S.K.; D.G. performed pre-processing; D.G. analyzed the data with the help of J.O. and M.A.G.; Z.Z. helped to maintain the experimental setup; D.G. wrote the manuscript with the help of T.E., T.S., J.O., M.A.G., and O.M.

Conflicts of interest. The authors declare no conflicts of interest.

Supplementary Material

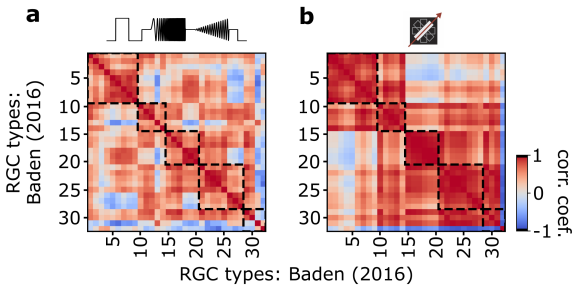

Fig. S1. Autocorrelation matrix of Baden et al. (2016) dataset. (a) Autocorrelation matrix of average type responses per RGC types of the Baden et al. (2016) dataset for responses to the chirp stimulus. Dashed boxes indicate functional groups (Off, On-Off, Fast On, Slow On, and Uncertain RGCs). Color bar indicates Pearson correlation correlation. **b** As (a), but in response to the moving bar stimulus.

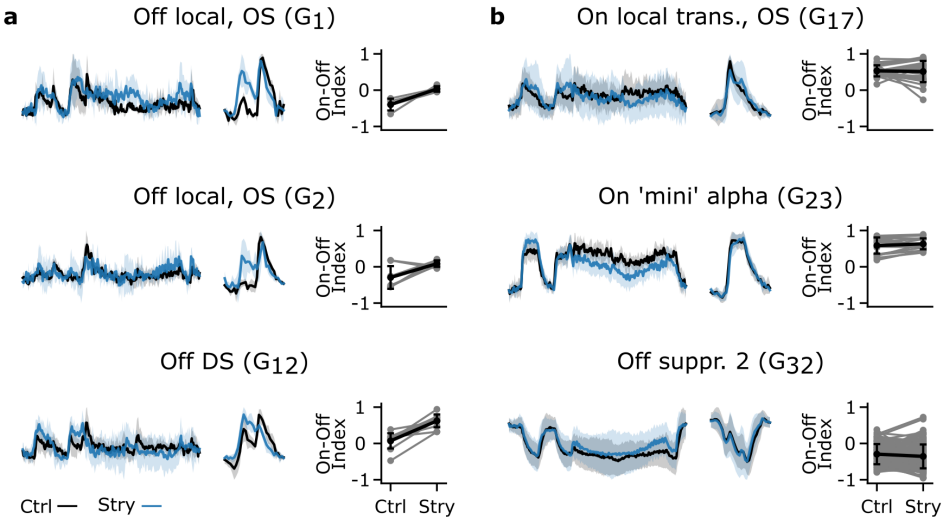

Fig. S2. Testing the effects of strychnine on different RGC type responses. (a) Left: Representative mean calcium responses of paired RGC types between Ctrl (black) and Strychnine-application (blue) (top: G_1; middle: G_2; bottom: G_{12}) exhibiting Off-responses. Right: Corresponding On-Off indices of paired RGCs for the Ctrl and Strychnine condition. **(b)** Left: As **(a)**, representative mean calcium responses of paired RGC types between Ctrl (black) and Strychnine-application (blue) (top: G_{17}; middle: G_{23}; bottom: G_{32}) exhibiting mainly On-responses and a suppressed-by-contrast component. Right: Corresponding On-Off indices of paired RGCs for the Ctrl and Strychnine condition.